Subsidence mechanisms and sedimentation in alluvial sinkholes inferred from trenching and ground penetrating radar (GPR). Implications for subsidence and flooding hazard assessment

Ivan Fabregat [a], Francisco Gutiérrez [a*], Carles Roqué [b], Mario Zarroca [c], Rogelio Linares [c], Xavier Comas [d], Jesús Guerrero [a], Domingo Carbonel [a]

[a] Departamento de Ciencias de la Tierra; Universidad de Zaragoza; C/. Pedro Cerbuna 12; 50009 Zaragoza; Spain
[b] Àrea de Geodinàmica Externa i Geomorfologia; Universitat de Girona; Campus Montilivi; E-17003 Girona; Spain
[c] Departamento de Geología; Universidad Autónoma de Barcelona; 08193 Barcelona; Spain
[d] Department of Geosciences, Florida Atlantic University, Davie, FL, USA

* Corresponding author Tel: +34 976 761090; Fax: +34 976 761106
E-mail address: fgutier@unizar.es (F. Gutiérrez)

Abstract

Sinkholes function as small sediment traps that may host valuable stratigraphic records for paleoenvironmental reconstructions and hazard assessments (e.g., subsidence, floods, hurricanes, tsunamis, tephra fall-out). The sedimentological features and completeness of such archives are~~is~~ influenced by the sedimentation and subsidence patterns and rates. However, karst depressions are frequently treated as static basins unaffected by settlement. This work illustrates the practicality of integrated studies combining trenching, numerical dating and shallow geophysical techniques (GPR) for characterizing the subsurface subsidence structure associated with sinkholes and reconstructing their deformational and sedimentary history. The approach is applied in two collapse sinkholes located in contrasting geomorphic settings (relict terrace and floodplain) related to deep-seated interstratal karstification of evaporites. The analysis of the sinkholes, particularly the trenching technique, provides practical information for assessing the associated subsidence hazard, including the presence of larger cavities at depth, the kinematic regime (episodic versus progressive), evidence of catastrophic displacement (fluidization structures) and the magnitude and timing of collapse events, especially the most recent one. The sinkhole located in the floodplain offers the opportunity of analyzing the possibilities and limitations of subsidence sinkholes as recorders of past floods in alluvial environments. This depression shows a largely incomplete record attributable to the high frequency of flood events compared to that of the collapse events, which create the accommodation space for sediment deposition. These limitations could be partially overcome by selecting old sinkholes situated in low terraces and/or affected by rapid subsidence.

Keywords: sinkhole sedimentation; subsidence history; sinkhole hazard; paleofloods

1. Introduction

Sinkholes or dolines are internally drained depressions characteristic of karst terrains underlain by carbonate or evaporite rocks. Two main groups of sinkholes can be differentiated from the genetic perspective (Gutiérrez, 2016): solution sinkholes generated by differential lowering of the ground by surficial dissolution, and subsidence sinkholes related to subsurface karstification and downward displacement of the overlying undermined material. Three main types of subsidence mechanisms may operate in the latter group: downward migration of cover deposits through subsurface voids and settling of the ground surface (suffosion); brittle deformation through the development of well-defined failure planes and/or brecciation (collapse); and downward bending of sediments above a karstification zone (sagging). The latter mechanisms typically occurs in evaporitic karst environments underlain by high solubility and ductile bedrock.

Sinkholes are enclosed depressions that function as sediment traps. They may host the only available stratigraphic record in erosional karst landscapes, typically dominated by internal drainage. Moreover, subsidence, either progressive or episodic, may favour the preservation of relatively long and complete stratigraphic records. The infill of adequately selected sinkholes and sinkhole lakes may provide valuable information for Quaternary studies and hazard analyses. Sinkholes have been widely used in retrospective investigations for (1) reconstructing paleoenvironmental and paleoclimatic variability (e.g., Laury, 1980; Whitmore et al., 1996; Hyatt and Gilbert, 2004; Hoddel et al., 2005; Morellón et al., 2009; Barreiro-Lostres et al., 2014; Perrotti, 2018; van Hengstum et al., 2018); (2) deciphering sea-level changes (Kovacs et al., 2013); (3) inferring the impact of past human activity on the landscape (Kulkarni et al., 2016); (4) studying paleontological and archaeological sites as well as faunal changes (Carbonell et al., 2008; Calvo et al., 2013; Zaidner et al., 2014; Gutiérrez et al., 2016); (5) inferring geoarcheological landscapes (Siart et al., 2010); (6) estimating long-term erosion rates and their temporal variability (Turnage et al., 1997; Hart, 2014). Sinkholes can be also used as a source of objective information for prognostic hazard assessments, including subsidence associated with the development of the sinkhole (Carbonel et al., 2014; Sevil et al., 2017; Gutiérrez et al., 2018); paleofloods (Gutiérrez et al., 2017); hurricanes (Gischler et al., 2008; Lane et al., 2011; Brown et al., 2014); tephra fall-out (Siart et al., 2010).

Sinkhole sedimentation is strongly influenced by the geomorphic setting (e.g., relict versus active geomorphic surface) and the subsidence patterns and rates. However, Quaternary studies focused on sinkhole-fill deposits frequently do not explore the impact of geomorphic factors on sedimentation. Moreover, in most cases sinkholes are considered as static basins in which variations in the position of their bottom is exclusively related to aggradation, and not to subsidence. However, subsidence events or temporal variations in the subsidence rates may induce significant changes in sedimentation regardless of the external environmental conditions. Previous investigations illustrate how detailed sinkhole-specific investigations, combining trenching, geochronological analyses and shallow geophysics provide critical data for assessing the subsidence hazard associated with them (Carbonel et al., 2014; Fabregat et al., 2017; Sevil et al., 2017). This work expands the practicality of applying those methods for unravelling the impact of various factors on sinkhole sedimentation and the characteristics of the associated stratigraphic archives, including the geomorphic setting and the subsidence patterns and rates. Two collapse sinkholes located in an interstratal karst environment and contrasting geomorphic settings (relict terrace; floodplain affected by frequent floods) were selected and studied combining detailed mapping, trenching, radiocarbon dating, and ground penetrating radar (GPR). The characterisation of the sinkholes and their comparison allows us to illustrate: (1) the practicality of combining trenching and GPR for resolving subsidence structures associated with sinkholes; (2) how the trenching technique, in combination with geochronological data and retrodeformation analyses can be used to reconstruct the deformation and depositional history of sinkholes and infer critical subsidence hazard parameters; (3) the impact of the geomorphic setting along with subsidence patterns and rates on sinkhole sedimentation and the completeness of the stratigraphic record; (4) the possibilities and limitations of sinkholes as recorders of past floods for flood-frequency analyses.

2. Geological, geomorphological and hydrological setting

The two investigated sinkholes, named the Anfiteatro sinkhole and the Fares sinkhole, are located in the middle reach of the Fluvia River valley, NE Spain (**Fig. 1**). This valley section has been excavated along the boundary between two major geological units separated by the E-W-trending and S-verging Vallfogona Thrust: the Pyrenean orogen to the north and the Ebro Cenozoic basin to the south (**Fig. 1B**). The hanging wall of the Vallfogona Thrust corresponds to the so-called Cadi Unit, which is the youngest and lowest thrust sheet of the eastern South Pyrenean Zone (Martínez et al., 1997; Barnolas and Pujalte, 2004). This structural unit includes formations of the Eocene South Pyrenean foreland basin that were incorporated into the orogenic wedge through a piggy-back propagation sequence (Puigdefàbregas et al., 1986). The footwall of the Vallfogona Thurst, where the two analysed sinkholes are located, corresponds to the northern sector of the Ebro Cenozoic basin (**Fig. 1B**). Here, the exposed bedrock is an autochthonous succession deposited in the Eocene South Pyrenean foreland basin and affected by gentle E-W-oriented folds (Martínez et al., 2000; Carrillo et al., 2014). The formations exposed in the footwall of the Vallfogona Thrust include the following Early-Middle Eocene stratigraphic units from base to top, recording an overall regressive trend (**Fig. 1C**) (Carrillo et al., 2014; Gutiérrez et al., 2016): (1) Beuda Gypsum (Early-Middle Eocene): this is an evaporitic unit up to 130 m thick deposited in a relatively shallow platform-like basin, mainly composed of white massive and crudely bedded gypsum (selenitic; nodular) with interbedded marls. The exposed secondary gypsum grades into anhydrite at depth. This is the soluble formation responsible for the generation of the studied sinkholes. (2) Banyoles Formation (Middle Eocene marls): This unit, locally more than 400 m thick, consists of poorly stratified bluish grey marls. It records relatively deep sedimentation in a pro-delta environment. (3) Bracons (or Coubet) Formation (Middle Eocene sandstone): This is a deltaic succession designated as Coubet Formation in the Pyrenees and Bracons Formation in the Ebro Basin. It consists of tabular well-bedded grey sandstones and claystones with some limestone intercalations. The Banyoles and Bracons formations are interdigitated, recording a S-directed fluvial system (Bracons/Coubet Fm.) that graded into deeper pro-delta environments with marl sedimentation to the south (Banyoles Fm.). (4) Besalu Gypsum (Middle Eocene): This is an evaporitic unit 5-25 m thick dominated by white gypsum and intercalated within the interfingered Banyoles and Bracons formations. (5) Bellmunt Formation (Middle Eocene): This is a red conglomeratic unit several hundred meters thick deposited in alluvial environments. Additional details on the geology of the study area can be found in Gutierrez et al. (2016, 2019).

A total of eight stepped terrace levels were mapped by Gutiérrez et al. (2016) in the middle reach of the Fluvia valley (T1: +91-97 m; T2: +75-82 m; T3: +47-53 m; T4: +36-45 m; T5: +28-32 m; T6: +19-25 m; T7: +8-12 m; T8: +3-7 m; height above channel), as well as five mantled pediments correlative to some of the oldest terraces (P1, P2, P3, P4, P6). The terrace T3 of the Fluvia River connects with the Sant Jaume lava flow, which in turn matches to the west with the upper basalt flow of Castellfollit, dated at 217-167 ka by Ar40/Ar39 (Lewis et al., 1998) (**Fig. 1B**). The two investigated sinkholes are situated at the southern bank of the Fluvia River on contrasting morpho-stratigraphic settings. The apparently inactive Anfiteatro sinkhole occurs on the Pleistocene terrace T5, whereas the active Fares sinkhole lies on the active floodplain (T8). The latter sinkhole functions as a sediment trap during flood events.

The Fluvia River catchment has an area of 974 km^2 and a relief of 1514 m, from the highest point of the divide to the river mouth in the Mediterranean Sea. It is characterised by a Mediterranean climate with subalpine features in the northern mountainous sectors. The average precipitation in the watershed ranges from 1165 mm to 630 mm and the mean annual temperature in the Olot meteorological station is 15.5ºC (Linares et al., 2017). The Fluvia River has an average discharge of 8 m^3/s at the Esponella gauging station, located ca. 5 km downstream of the investigated area and with a contributing area of 804 km^2. This unregulated fluvial system with no reservoirs experiences frequent floods, mainly concentrated in autumn when frontal rainfall events are more frequent (Meteocat, 2018). Table 1 includes a compilation of historical damaging floods recorded in the middle reach of the Fluvia River from the Middle Ages.

3. Methodology

Initially, detailed geological-geomorphological maps of the sinkhole sites were produced using previous cartographic works (Mató et al., 1996; Roqué et al., 1999; Martínez et al., 2000; Carrillo et al., 2014; Gutiérrez et al., 2016) and conducting thorough field surveys. Available borehole data provided some information on the position of the alluvium-bedrock contact and the top of the evaporites (e.g., Barberà and Buxó, 1998; Roqué et al., 1999; ICC, 2001, 2010; ICGC, 2018). The water-table depth was measured in some wells with a portable water level logger. Historical imagery available in Google Earth Pro and the viewer of the Institut Cartogràfic i Geològic de Catalunya were also used to recognize recent variations of the analysed sinkholes, chiefly related to human activity.

GPR data was acquired along one line across the Anfiteatro sinkhole and two perpendicular lines centered in the Fares sinkhole. Each line was replicated with a RIS system (Ingegneria dei Sistemi) using bistatic 40 MHz (unshielded), 100 MHz (shielded) and 200 MHz (shielded) antennas in common offset mode. One Common-Midpoint (CMP) profile was acquired at the Anfiteatro site and two in the Fares site by separating stepwise the transmitter and receiver 100MHz antennas. These data were used to estimate subsurface velocities (e.g., Annan, 2009). GPR data was processed with the software ReflexW 8.5 (by Sandmeier geophysical research; www.sandmeier-geo.de) applying the following work flow: (1) a one-dimensional dewow to eliminate low frequency (wow) components; (2) static correction to compensate for the time delay of the first arrival; (3) background removal to remove high-frequency noise; (4) a time-varying gain to amplify late travel-time signals; (5) bandpass frequency filter to increase the signal-to-noise ratio; (6) Stolt migration using a single velocity of 0.095 m ns-1 and 0.105 m ns-1 for the Anfiteatro and Fares sites, respectively, derived from CMP data; (7) topographic correction.

Field Code Changed

Backhoe trenches 32 m and 47 m long were excavated in the Anfiteatro and the Fares sinkholes, respectively, which were partially coincident with GPR profiles for direct comparison. The Anfiteatro trench was extended from the center to the margin of the depression, whereas the Fares sinkholes covered the full collapse structure. The trench walls were cleaned and one of them was gridded with horizontal and vertical strings. The selected wall was logged on graph paper at a scale of 1:50 after marking stratigraphic contacts and faults with color pins. A total of 13 samples from key stratigraphic units were sent for AMS radiocarbon dating, of which 3 had insufficient charcoal for dating. The obtained conventional radiocarbon ages were calibrated to calendar ages using the

Calib7.1 software (Stuiver and Reimer, 1993; Stuiver et al., 2017) and the IntCal 13.14c calibration data set (Reimer et al., 2013) (**Table 2**).

4. The Anfiteatro sinkhole

4.1. Description of the sinkhole and setting

The apparently inactive Anfiteatro sinkhole covers 3,908 m^2 and has a NE-oriented elongated shape, 79 m long and 67 m wide (**Fig. 2**). It is a scarped edge depression ca. 15 m in maximum depth, with a flat floor used for cultivation and an estimated volume of 41 10^3 m^3. The margins of the sinkhole show a sequence of benches that led some archeologists to interpret the enclosed depression as the ruins of a Roman amphitheater with a capacity for 4000 people (Burch et al., 2014). They ascribed the staircased margins to annular corridors of a supposed grandstand (*praecinto*), and the more degraded low-relief NE edge to the access to the central arena. However, a recent archeological investigation, including the excavation of test pits, ruled out the Roman amphitheater interpretation and proposed that the stepped margins correspond to artificial terraces with masonry walls aimed at improving the stability of the slopes (Casas et al., 2016).

The Anfiteatro collapse sinkhole formed on the tread and riser of terrace T5 of the Fluvia River, dominated by gravel facies and perched around 30 m above the river channel (Roqué et al., 1999; Gutiérrez et al., 2016) (**Fig. 2**). This terrace is younger than 217-167 ka, which is the age ascribed to the older terrace T3 on the basis of Ar^{40}/Ar^{39} dating of basalts in Castellfollit village (Lewis et al., 1998; Gutiérrez et al., 2016). The exposed bedrock in nearby outcrops to the south corresponds to the Banyoles Marls (Martínez et al., 2000). A borehole drilled on terrace T4 west of the sinkhole penetrated Banyoles Marls up to a depth of 93 m without reaching the top of the Beuda Gypsum. This information indicates that the Anfiteatro sinkhole is related to deep-seated interestratal karstification of the Beuda Gypsum beneath a thick caprock of Banyoles Marls mantled by Quaternary alluvium.

The Anfiteatro sinkhole was depicted in an old topographic map produced by Papell i Llenas (1862) for the Besalu City Hall at 1:2,000 scale, providing a minimum bracketing age for the depression. Old grey-scale aerial photographs from 1946 suggest that the sinkhole floor is affected by ponding. This can be attributed to perched ephemeral water accumulated on the clayey bottom of the depression (**Fig. 2B**). Here, the depth of the water table was measured in June and July 2016 at 15 m and 20 m, respectively.

4.2. The Anfiteatro trench

A 32 m long and 4.4 m deep trench was excavated in the Anfiteatro sinkhole. The trench, with a N34E orientation, was dug from the NE margin of the depression towards its center (**Fig. 2**). It crossed the degraded marginal scarp associated with the riser of terrace T5 and was extended radially across the subcircular crop field situated in the bottom of the depression, with a gentle inward slope of 2°. The excavation exposed an inward-dipping collapse fault and three main sedimentary packages, two of them faulted and a younger unconformable one that truncates the fault (**Fig. 3**):

(1) Package I (units 1 to 5), only exposed in the footwall, consist of faulted indurated gravelly deposits of terrace T5.

(2) Package II (units 6 to 9), with an exposed thickness of 3.3 m, corresponds to faulted sinkhole-fill deposits confined to the downthrown block. This package is dominated by tabular clay units, and includes poorly exposed gravelly colluvial facies juxtaposed to the fault (unit 8). The upper clayey unit 9 shows a gravel pocket 0.5 m across situated 1 m apart from the collapse fault. This feature is indicative of penecontemporaneous soft-sediment deformation, probably related to liquefaction (Postma, 1983; Johnson, 1986; Nocita, 1988). Three charcoal samples collected from this package at 15 cm, 75 cm and 140 cm below the top of the package yielded ages in correct stratigraphic order of 80-231, 330-433, and 599-668 cal. yr AD (age ranges at 2 sigma) (**Table 2**).

(3) Package III (units 10 to 15), 2 m thick in the trench, is a non-deformed sinkhole fill that onlaps the collapse fault and package I. This package consists of interbedded and interdigitated gravelly and fine-grained units, and is capped by a laterally continuous anthropogenic unit (unit 15, agricultural soil). In the fault zone, this package lies on a subtle angular unconformity over packages I and II, the latter affected by drag folding.

Towards the central sector of the sinkhole, the units of packages II and III show an apparent conformable relationship (parallel unconformity) related to limited internal deformation in the lower package. Two charcoal samples collected from this package at 60 cm and 240 cm below the ground surface yielded ages of 663-777, and 1274-1391 cal. yr AD, respectively (age ranges at 2 sigma) (**Table 2**).

Interestingly, the observable deformation is concentrated within a narrow zone around 3 m wide associated with the marginal collapse fault (**Fig. 3**). In the rest of the trench the strata show an apparent subhorizontal attitude. The fault juxtaposes the terrace deposits and the older sinkhole fill and shows an inward dip of 75°. It is expressed as a shear zone 20 cm wide in which the clasts show reoriented fabrics. The sediments abutting the fault are affected by drag folding. The terrace deposits in the footwall are bent downwards in a 1.3 m wide drag fold with a throw of 0.25 m and a local dip of 15°. The drag fold in the older sinkhole fill is not fully exposed.

The available numerical ages, all of them in correct stratigraphic order, allow the estimation of various sedimentation rates considering the thickness of the deposits between the sampling points and maximum and minimum time spans given by the corresponding age ranges. The oldest and youngest ages from package II (1.5 m) yield a sedimentation rate of 2.5-4.1 mm/yr. The oldest (package II) and the youngest ages (package III) of the trench (3.2 m) provide a deposition rate of 2.4-2.7 mm/yr (**Fig. 4**). An aggradation rate of 1.8-2.0 mm/yr can be also estimated considering the oldest age and the thickness of the overlying sediments up to the surface (3.6 m).

The stratigraphic and structural relationships observed in the trench allow us to infer the following stepwise evolution for the Anfiteatro collapse sinkhole, which is illustrated in the retrodeformation sequence shown in **figure 5:** (1) Initiation of the formation of the Anfiteatro sinkhole by a collapse developed on terrace T5. This event generated the accommodation space for deposition of package II, more than 3.3 m thick. Probably, the sinkhole has been affected by more than one collapse event before the sedimentation of package II. However, the trench does not have sufficient depth to expose the base of the sinkhole fill, providing an incomplete record. (2) Deposition of package II. (3) New collapse event that faulted and downdropped package II, creating additional accommodation space for deposition of package III. Most probably the gravel pocket mapped next to the fault and in the upper part of package II was formed during this event, due to local dynamic loading induced by a rapid collapse. The exposed thickness of package II provides a minimum estimate of 3.3 m for the vertical displacement achieved in this event. The timing of this event can be constrained within 599-777 cal yr AD with samples collected just beneath and above the event horizon. (4) Coeval degradation of the marginal scarp and deposition of package III, which includes material derived from the sinkhole edge. The lack of a well-developed colluvial wedge at the base of this package and next to the fault may be attributed to the high resistance of the hardened terrace deposit, with a repose angle higher than the slope of the scarp generated by the collapse event. During this final stage human activity may have contributed to modify the topography. especially at the trench site, which is used as the access point to the crop field.

4.3. GPR survey at the Anfiteatro sinkhole

A total of three GPR profiles were acquired across the Anfiteatro sinkhole using two shielded antennas (100 MHz and 200 MHz) and an unshielded antenna (40 MHz). The profiles were partially coincident with the trench for direct comparison. Overall, the GPR results were rather poor, mainly due to signal attenuation caused by the electrically conductive clayey sinkhole fill. Moreover, the GPR data obtained with the 40 MHz unshielded antenna were strongly contaminated by above-surface reflections, notably those derived from a high-voltage cable located over the NE margin of the sinkhole. In this work, for brevity, we show the radargram obtained with the 100 MHz antenna, which vaguely images some of the geometrical features observed in the trench (**Fig. 6**). This profile shows a penetration depth of around 5 m, slightly higher than the trench. The inward-dipping marginal collapse fault is expressed by lateral interruptions of some reflections and a lateral change in the reflection pattern. The stratified terrace deposits in the footwall (package I) produce strong and laterally continuous reflections. They apparently show an inward dip next to the fault, coherent with the drag fold observed in the trench. In contrast, the massive and clay-rich faulted sinkhole fill (package II) is expressed by attenuated, discontinuous and wavy reflections. The non-faulted gravelly and crudely bedded sinkhole fill is shown as well-defined, laterally continuous reflections along the whole profile and across the fault zone. This package displays a concave base, with a maximum thickness of 3-4 m in the sinkhole center. Despite the data being acquired with a shielded antenna, a diffraction hyperbola derived from the high-voltage cable partially contaminates the profile in the margin of the sinkhole.

5. The Fares sinkhole

5.1. Description of the sinkhole and setting

The Fares sinkhole is located on the lowermost terrace (T8) of the Fluvia River, around 150 m distant from the active channel (**Fig. 7**). This terrace lies at around 3 m above the gravelly river channel on its southern bank, and is periodically affected by flooding (floodplain). The sinkhole is expressed at the surface of a crop field as a subcircular depression with vaguely-defined edges, it is 30 m in diameter and 0.4 m deep, apparently resembling a sagging sinkhole related to the downward flexure of the alluvial cover. Historical imagery available at some cartographic viewers (e.g., Google Earth Pro, Institut Cartogràfic de Catalunya) reveals that the sinkhole already existed in 2006 shown by a subcircular area in the crop field with a different tone).

According to the available cartographic data, the Fares sinkhole is located in the footwall of the Vallfogona Thrust (**Fig. 7**), and the bedrock underlying the Quaternary alluvium corresponds to marls of the Banyoles Formation, like in the Anfiteatro sinkhole (Martínez et al., 2000; Gutiérrez et al., 2016). The Banyoles Marls are exposed in an outcrop located 500 m to the SE of the sinkhole. This exposure shows a caprock and cover sagging paleosinkhole more than 300 m across, affecting to both the Banyoles Marls and the Quaternary alluvium. Here, the sagged Quaternary cover is anomalously thick (ca. 50 m) and includes a unit of palustrine marls tens of meters thick, recording synsedimentary subsidence that generated palustrine environments in the valley floor (Gutiérrez et al., 2016). These data indicate that karstic subsidence in the Fares site is related to interstratal dissolution of the Beuda Gypsum beneath a caprock of Banyoles Marls, extensively mantled by an alluvial cover.

5.2. The Fares trench

A 47 m long and 2.6 m deep trench was excavated across the Fares sinkhole (**Figs. 8, 9**). The trench had an E-W orientation approximately parallel to the E-directed Fluvia River valley, with the western and eastern sectors associated with the upstream and downstream edges of the depression, respectively (**Fig. 7**). The excavation exposed an entire collapse structure 24 m across bounded by well-defined dip-slip faults. The recent sinkhole fill comprises various flood sequences that show an overall asymmetric synformal structure with upward-dip attenuation. The exposed sedimentary units can be grouped into four packages bounded by failure planes and major depositional discontinuities (i.e., sequence boundaries):

(1) Package I (terrace deposit; units 1 and 2), exposed on the margins of the sinkhole (in situ) and in the western edge of the collapse structure (downthrown), consists of rounded polymictic gravels (unit 1, channel facies) overlain by a laterally discontinuous bed of bioturbated silty sands with granules. A charcoal sample collected from unit 1, 0.3 m below the top of the unit, has yielded a calibrated radiocarbon age of 1296-1403 cal. yr AD.

(2) Package II (1st flood sequence; units 3 to 5), located at the sinkhole margins and within the collapse structure, corresponds to a fining-upwards flood sequence 0.7-0.9 m thick comprising distinctive beds. On the western (upstream) margin of the sinkhole, this package includes from base to top (1) horizontally laminated coarse sand with granules (unit 3); (2) massive medium sand (unit 4); and (3) massive, bioturbated sandy silt with abundant snails (unit 5). The lower laminated coarse sand bed of the flood sequence is missing within the collapse structure and on the downstream margin of the depression. A charcoal sample collected from unit 4 in the foundered succession has provided a calibrated age of 1445-1631 cal. yr AD.

(3) Package III (2nd flood sequence; units 6 to 8) is a flood sequence more than 1.7 m thick restricted to the sinkhole fill. It shows an asymmetric facies distribution, with units 6 and 7 grading into unit 8 towards the downstream sector of the sinkhole through a gradational lateral facies change. Overall, this package displays upward- and downstream-fining trends. The basal unit 6 is made up of coarse sand with scattered granules, whereas units 7 and 8 consist of sandy silt. A charcoal sample collected 70 cm below the top of the package has yielded calibrated radiocarbon ages of 1690-1925 cal. yr AD.

(4) Package IV (3rd flood sequence; units 9 and 10) is also confined to the sinkhole and is the youngest flood sequence reaching 1.9 m in thickness. Its lower unit 9 consists of multiple sets of low-angle cross-laminated sand dipping downstream. The upper unit comprises a bed of massive fine sand overlain through a gradational contact by massive, bioturbated silt. Two samples collected 5 cm and 55 cm above the base of the package have provided calibrated ages of 1653-1952 cal. yr AD and 1660-1953 cal. yr AD, respectively. The ground surface along the entire length of the trench is underlain by a 0.2-0.5 m thick agricultural soil disturbed by tillage (unit 11).

The collapse structure is bounded by well-defined normal faults that most likely correspond to a single annular collapse fault (ring fault). Interestingly, the loose outer sediments of the collapse (footwall) show a horizontal attitude and are barely affected by fault dragging. The eastern fault is defined by a subvertical shear zone with reoriented fabrics as much as 50 cm wide, with an associated fissure 30 cm wide in the upper part. The fissure is filled by a chaotic admixture from units 5 and 10b and truncated by the agricultural soil. The fault, with a minimum throw of 2.4 m, clearly offsets packages I to III, whereas package IV seems to be solely affected by the horizontal separation of the fissure.

The western fault has an inward dip of 70° and a throw of 1.3 m as measured at the top of unit 1. This western fault also offsets packages I to III and is overlapped by package IV. The fault shows a shear zone and a splay of steeper microfaults that terminate at the base of package III. The internal structure of the foundered block displays an asymmetric synform with a steeper eastern limb and the axis situated at 4 m from the eastern fault. This inner folding structure corresponds in 3D to a basin structure with centripetal dips. Overall, the dip of the sediments of the sinkhole fill attenuates upwards. Although the trench does not expose the base of the sinkhole fill, the structural relief of the synform can be constrained between 2.1 m and 5.1 m extrapolating the top of unit 1 to the hinge of the synform with the geometry of the base of unit 9 and with the dip of unit 1 in the downthrown block, respectively.

A retrodeformation analysis carried out with the geometrical and geochronological data obtained from the trench, and assuming that deposition during each flood event tends to completely fill the sinkhole, indicates the following sequence of subsidence and depositional events (Fig. 10):

(1) Deposition of package I in the medieval period sometime around 1296-1403 cal. yr. AD, when the active Fluvia River channel used to be situated at the sinkhole site. (2 and 3) Probable initiation of the sinkhole and deposition of the first flood sequence (package II) across the depression at 1445-1631 cal. yr AD. The presence of a depression during this depositional event is weakly supported by the fact that the horizontally laminated sand (unit 3) only occurs on the upstream margin of the sinkhole, suggesting that the depression locally changed hydraulic conditions due to flow separation. Potential thickness changes within this package are not observable due to the limited depth of the trench. (4 and 5) Subsidence event by collapse faulting and internal sagging with a vertical displacement greater than 1.7 m and deposition of the second flood sequence (package III) restricted to the sinkhole depression. The depth of the sinkhole at this stage was significant enough to control the depositional style and lateral facies changes across the sinkhole. The timing of the deposition event can be roughly situated at 1690-1925 cal. yr AD. (6 and 7) Additional subsidence event with a magnitude of 1.9 m at the trench, and deposition of the flood sequence corresponding to package IV sometime within the age range 1690-1953 cal. yr AD. (8) Opening of an extensional fissure on the eastern margin of the sinkhole and its infill. This local surface deformation was not necessarily related to the reactivation of the sinkhole. It could be caused by shallow compaction and contraction of the sinkhole-fill deposits, which reach higher thickness on the eastern half of the depression. (9) Development of an agricultural soil by tillage and obliteration of the upper part of the fissure.

Overall, the trench records two subsidence mechanisms: (1) vertical displacement on the marginal collapse fault, with a minimum throw of 2.4 m on the eastern edge; and (2) downward flexure within the foundered block with a loosely estimated structural relief of 2.1-5.1 m. Several options can be considered for the timing of the sinkhole initiation: (1) before deposition of package II, sometime after 1296 yr AD; (2) after deposition of package II, whose age is bracketed at 1445-1631 cal. yr AD. With these poorly constrained numerical ages and considering a cumulative vertical subsidence between 4.5

m and 7.5 m, we can calculate long term subsidence rates ranging between 7.8 mm/yr - 96 mm/yr, much higher than those estimated in the Anfiteatro sinkhole. Stratigraphic and structural relationships indicate a minimum of two subsidence episodes, each with vertical displacements ≥1.7 m. The sinkhole formation/reactivation episodes created the accommodation space for the accumulation of deposits confined to the depression during two subsequent flood events. Unfortunately, the available radiocarbon ages, due to the shape of the calibration curves do not allow precise determination for the timing of these palaeofloods, both occurred within a time interval of 263 yr (1690-1953 cal. yr BP).

5.3. GPR survey at the Fares sinkhole

A total of six GPR profiles were acquired across the Fares sinkhole along two lines. One of the them 480 m long and parallel to the trench, and the other one 240 m long and perpendicular to the trench (**Fig. 7**). The profiles were replicated along these lines using two shielded antennas (200 MHz and 100 MHz) and an unshielded antenna (40 MHz). All the radargrams clearly capture the sinkhole, offering better results than at the Anfiteatro sinkhole. The highest-quality profiles are those obtained with the 200 MHz antenna due to their higher resolution. The potential higher penetration of the lower frequency antennas was limited by the shallow water table in this floodplain environment, situated at 3.5 m depth, as measured in an adjacent water well and imaged in the radargrams. **Figure 11** illustrates the central portion of the 200 MHz profile acquired parallel to the trench and slightly displaced to the north. The margins of the collapse structure can be recognized through laterally truncated reflections and by an abrupt change from subhorizontal to dipping reflections. These inward dipping reflections and the associated collapse faults can be traced up to the bottom of the profile. Within the subsidence structure, consistently with the geometries observed in the trench, the reflections show an asymmetric synform with a steeper and shorter eastern limb. The inclined reflections show upward-attenuating dips, and are onlapped by shallow subhorizontal reflections. This is coherent with the inferred episodic evolution of the sinkhole, in which older sediments have accommodated a higher amount of deformation. Moreover, the profile shows slightly lower penetration in the sinkhole zone, where the fined-grained sinkhole fill, with higher electrical conductivity than the marginal gravels, attenuates the electromagnetic waves. The apparent smaller size of the sinkhole imaged in this GPR profile (15-20 m) compared to that measured in the trench (24 m) can be attributed to the fact that the GPR line was displaced a few meters from the major axis of the depression.

6. Discussion

6.1. Subsidence structure and deformation history

Detailed geological mapping and local borehole data indicate that the two investigated sinkholes are related to the interstratal karstification of the Beuda Gypsum beneath a caprock a few tens of meters thick of Banyoles Marls, which is mantled by Quaternary alluvium. The sinkholes are located in markedly different geomorphic settings that strongly control sedimentation processes and rates, and probably also subsidence mechanisms. The Anfiteatro sinkhole occurs on an indurated terrace perched around 30 m above the Fluvia River (**Fig. 2**), whereas the Fares sinkhole lies on the floodplain, underlain by soft recent alluvium (**Fig. 7**).

Trenching and geophysical data indicate that the 80 m long Anfiteatro sinkhole does not correspond to a Roman amphitheater, as initially proposed (Burch et al., 2014), but to a caprock and cover collapse sinkhole following the classification of Gutiérrez et al. (2008). The collapse structure is controlled by a steep, inward-dipping and well-defined annular fault and the downthrown block shows very limited internal deformation within the investigation depth of the trench (**Fig. 3**). In this sinkhole, the performance of the GPR technique was very poor due signal attenuation related to the presence of a highly electrically conductive clayey fill, and did not allow to obtain information on the total thickness of the sinkhole-fill deposits (**Fig. 6B**).

The trench excavated across the Fares sinkhole revealed a full collapse structure bounded by a well-defined and steeply-dipping ring fault ca. 24 m wide (**Figs. 8, 9**). However, in this case, the soft alluvium displayed significant internal ductile deformation, accommodated through the development of an eccentric basin structure with centripetal dips. Both collapse faulting and sagging substantially contribute to the overall subsidence magnitude, loosely constrained at 4.5-7.5 m. This sinkhole can be classified as a caprock and cover collapse-sagging sinkhole (Gutiérrez et al., 2008; Gutiérrez, 2016). In the Fares sinkhole the GPR profiles, especially those acquired with the high-frequency antennas, which yield higher resolution, imaged the collapse and sagging structures, reveled by lateral truncations, sharp dip changes and the synform (**Fig. 11A**). The better performance of this method compared with the Anfiteatro sinkhole can be attributed to the lower amount of clay in its fill and the dominance of gravels in the encasing sediments.

The stratigraphic and structural relationships observed in the trenches provide some practical information on the kinematic style of the sinkholes and their subsidence history. Both sinkholes show unambiguous evidence of episodic displacement, revealed by upward fault truncations (Anfiteatro trench; **Fig. 3**) and different generations of faults overlain by successively younger non-faulted units (western margin of the Fares sinkhole; **Figs. 8, 9D**). Similar geometrical relationships indicative of stick-slip displacement have been documented in other sinkholes (e.g., Gutiérrez et al., 2009; Youssef et al., 2016; Fabregat et al., 2017). This kinematic regime, whereby relatively long periods of quiescence are punctuated by subsidence episodes, is the expected behavior for sinkholes in which deep-seated cavities are propagated through a thick and relatively rigid caprock. The gravel pocket observed in the collapsed sinkhole-fill deposit within the Anfiteatro sinkhole provides evidence of catastrophic displacement (**Figs. 3, 5**). This type of soft-sediment deformation has been documented in various depositional environments and attributed to fluidization processes favored by various factors, such as high sedimentation rates, poor sorting and granular deposits with contrasting permeability and density (Postma, 1983; Johnson, 1986; Nocita, 1988). In the Anfiteatro sinkhole, the pore-fluid overpressure that led to the fluidification of the water-saturated unconsolidated deposit was most probably induced by local dynamic loading associated with a sudden collapse event. Geometrical relationships observed in the Anfiteatro trench indicate a minimum of two subsidence events: the event that generated the sinkhole and the accommodation space for sedimentation and the most recent event (MRE) responsible for the fluidization structure, whose timing is constrained at 599-777 cal. yr AD (**Fig. 5**). Most probably, the actual number of subsidence events is much larger considering minimum subsidence magnitude given by the depth of the sinkhole (15 m) and the minimum thickness of the sinkhole fill (4.3 m). Interestingly, this sinkhole was not reactivated during the 1427-1428 Olot seismic crisis, which killed around 800 people in the region and included an event

(2 February, 1428) felt at the site with EMS-98 intensity VIII (Martínez-Solares and Mezcua, 2002).

The Fares sinkhole, developed in the floodplain of the Fluvia River valley is much younger. The trench records 2 or 3 subsidence events and the total subsidence has been estimated within 4.5-7.5 m (**Figs. 8, 10**). The timing of the putative oldest event, based on relatively weak evidence (i.e., facies change in the first flood sequence), can be constrained at 1296-1631 cal. yr AD. This age range includes the 1427-1428 seismic crisis, caused by the Amer Fault situated 20 km to the west; a coseismic sinkhole? (Perea, 2009). The age of the penultimate event (PE) and the most recent event (MRE), with displacements per event higher than 1.7 m, are loosely bracketed with the available radiocarbon ages at 1445-1925 cal. yr AD and 1690-1953 cal. yr AD, respectively.

6.2. Sinkhole sedimentation

The two investigated sinkholes display contrasting sedimentation styles conditioned by the geomorphic setting and the subsidence/aggradation ratio, which in the case of the Fares sinkhole is determined by the temporal frequency of the collapse and flooding events. The Anfiteatro sinkhole, situated on a perched terrace, behaves as a starved basin with a subsidence/aggradation ratio >1. In this depression, with a depth of around 15 m, slow deposition dominated by rather continuous accumulation of clayey facies by sheet wash is unable to counterbalance the accommodation space formed by subsidence. The chronological model constructed with five numerical ages indicates a sedimentation rate ranging between 1.8-4.1 mm/yr.

In the Fares sinkhole, located in the floodplain, the stratigraphy and retrodeformation sequence indicate episodic sedimentation during flood events. Here, the sedimentation rate (7.8-11.5 mm/yr) is limited by the creation of accommodation space by subsidence events. The depositional events are recorded by stacked fining-upward flood sequences 1-2 m thick that tend to be confined to the sinkhole depression. The basal unit may consist of low-angle cross-laminated sand, horizontally laminated sand or structureless and graded coarse sand with scattered granules. These facies are related to rapid deposition by sediment-laden traction currents, whose velocity sharply decreases at the sinkhole due to local flow depth increase and flow separation. Deposition of horizontally laminated sand and low-angle cross-laminated sand occurs under upper plane bed conditions with high-velocity flow, at the transition from the subcritical to supercritical regime (Ashley, 1990; Miall, 1996). These basal units are overlain by massive and strongly bioturbated silt- and clay-rich facies deposited during the waning stage of the floods by suspended load fall-out and some traction. The high concentration of low-density buoyant particles (e.g., snails, charcoal) indicates very low flow velocity and probably stagnation. These sediments are subjected to bioturbation until the subsequent aggradational flood event. Despite the limited size of the Fares sinkhole, the trench, excavated parallel to the flow direction, shows facies changes across the sinkhole, with coarser-grained and better stratified deposits in the upstream sector. Similar flood sequences have been documented in ponded zones of backflooded bedrock tributaries affected by high-stage floods (Benito et al., 2003).

Three flood events have been identified and dated in the infill of the Fares sinkhole (**Fig. 10**): (1) the first flood recorded by package II deposited across the sinkhole (1445-1631 cal. yr AD); (2) the second flood corresponding to package III, confined to the sinkhole (1690-1925 cal. yr AD); and (3) the third flood whose deposits are also restricted to the sinkhole (package IV; 1690-1953 cal. yr AD). The timing of the floods is poorly constrained by the available geochronological data and the determined age ranges for the two youngest events have overlapping ages, with higher probabilities according to the calibration curves for the period 1722-1879 cal. yr AD (see probabilities in **Table 2**). These data roughly indicate a recurrence for the stratigraphically recorded flood events of more than 100 years (three events since 1445-1631). However, historical data indicate that the site has been affected by a much larger number of flood events (see **Table 1**). Moreover, hydraulic modelling indicates that the sinkhole is located within the area affected by 40 yr return-period floods (ACA, 2018). This supports the interpretation that the recorded floods were those that occurred when there was accommodation space in the sinkhole created by a subsidence event. The topographic depression functions as a sediment trap that disturbs hydraulic conditions (i.e. flow separation) favoring rapid deposition. Flood events may not be recorded if they occur when the sinkhole is buried by deposits accumulated during a previous flood. This indicates that the completeness of the flood record depends on the relative recurrence of subsidence and flood events. The flood record in the Fares sinkholes is largely incomplete because subsidence events are less frequent than flood events.

6.3. Hazard implications

The presented analysis illustrates how the integrated analysis of specific sinkholes combining detailed mapping, trenching and GPR provide relevant information for hazard assessment. Trenching allows the precise identification of the edge of the subsidence structures. In some evaporitic areas subsidence structures tend to have much larger dimensions than the sinkhole depressions mapped on the basis of geomorphic criteria, due to the presence of a difficult-to-recognize aureole affected by subtle downward bending (Gutiérrez et al., 2018). However, in the Anfiteatro and Fares sinkholes, both involving the foundering of a thick competent caprock, subsidence is restricted to the collapse structure defined by a well-defined ring fault.

A relevant component of the severity (i.e., capability of a hazardous process to cause damage) associated with subsidence sinkholes is their kinematic regime, either progressive or episodic. Both sinkholes are characterized by episodic subsidence, and the Anfiteatro sinkhole shows evidence of catastrophic events recorded by sediment fluidization. Nonetheless, the geochronological data provide a valuable quantitative basis for assessing the probability of new subsidence events. The Anfiteatro sinkhole can be considered as an inactive or dormant depression since the MRE occurred around 1500 years ago (599-77 cal. yr AD) and it was not reactivated during the 1427-1428 Catalan seismic crisis that had a maximum epicentral intensity VIII at the site. The Fares sinkhole can be considered as active, although with a relatively low annual probability ~~of~~ being affected by new collapse events. This sinkhole has experienced two events with poorly constrained ages younger than 1445 cal. yr AD, both with vertical displacement higher than 1.7 m.

The Fares sinkhole provides the opportunity to assess the potential of sinkhole fills as archives of past flood histories in alluvial systems. Sinkholes are potentially suitable recorders of paleofloods since they behave as sediment traps, modify hydraulic conditions favoring rapid deposition; sediments may include abundant datable material, and subsidence contributes to the preservation of the flood deposits (Gutiérrez et al., 2017). However, the available historical and geological data illustrates that they may have significant limitations: (1) sinkhole depressions tend to be obliterated by rapid deposition during floods; (2) the flood record may be largely incomplete when the sinkholes are not affected by continuous subsidence or the recurrence of the subsidence events is lower than that of the floods; (3) the temporal length of the flood histories is restricted by the age of the sinkhole; (4) the resolution of radiocarbon ages may be insufficient to resolve the timing of flood events and estimate their temporal frequency. Some of these limitations can be partially reduced for the investigation of large low-frequency paleofloods by selecting old sinkholes located in low terraces and preferably affected by continuous subsidence.

7. Final considerations

Karst sinkholes function as sediment sinks and their stratigraphic record may provide valuable information for Quaternary studies (e.g., paleoenvironmental variability, fossil and archaeological sites) and hazard assessments. Subsidence, either progressive or episodic, may favour the preservation of relatively long, datable and continuous successions in areas dominated by erosion and with limited stratigraphic archives. These depressions may be used as recorders not only of the local subsidence associated with them, but also of other regional hazardous processes such as floods, tsunamis, hurricanes or tephra fall.

The completeness of the stratigraphic record in subsidence sinkholes, and consequently their usefulness for paleoenvironmental and hazard analyses, depends on the ratio between the aggradation and subsidence rates and their patterns. Sinkholes located on relict surfaces characterised by low sedimentation rates and aggradation/subsidence ratios <1 (starved basins) (e.g., Anfiteatro sinkhole), may host long and continuous stratigraphic records. In contrast, sinkholes lying on active geomorphic surfaces with high aggradation rates (e.g. Fares sinkhole) will tend to have short and discontinuous stratigraphic records (aggradation/subsidence>1), unless they are affected by rapid subsidence. These sinkholes (overfilled basins) are rapidly obliterated by accumulation and erosion processes. These factors should be taken into account when selecting sinkholes for Quaternary and hazard studies and interpreting their sedimentary fill.

The investigation conducted in two collapse sinkholes located in contrasting geomorphic settings (i.e., perched terrace and floodplain) and related to interstratal karstification of evaporites illustrates that GPR and trenching in combination with geochronological analyses, are suitable complementary techniques for unravelling the origin of karst depressions, determining their shallow subsurface structure and reconstructing their deformational and sedimentary history. The application of this integrated approach can be highly useful for paleoenvironmental studies focused on sinkhole-fill deposits. GPR is frequently adversely affected by the presence of electrically conductive clayey deposits, which cause severe attenuation of the signal limiting the effective investigation depth. However, under adequate conditions it allows the collection of spatially-dense information on subsurface stratigraphic and structural features in a non-intrusive fashion and with limited effort.

Trenching is a very advantageous method for sinkhole characterisation. A straightforward application of this technique yields abundant objective information on the stratigraphy and subsidence phenomenon, including the limits of the deformation zone, subsidence magnitude, subsidence mechanisms and their share, or the kinematic regime, either progressive or episodic. Both the Anfiteatro and the Fares trenches show geometrical relationships indicative of episodic displacement (e.g., upward fault truncations), and a fluidization structure exposed in the Anfiteatro trench points to a catastrophic displacement event capable of creating local pore-fluid overpressure conditions. A more elaborate and costly application of the trenching technique, including numerical dating and retrodeformation analyses, provides additional data on critical hazards parameters, including long-term subsidence rates, the timing of subsidence events, especially the MRE, and recurrence. This information provides an objective basis for assigning activity classes (e.g., active, dormant, relict) and forecasting the future behaviour of specific problematic sinkholes.

Generally, alluvial environments are unsuitable settings for the preservation of long and complete geological records of paleofloods. Subsidence sinkholes in alluvial settings could serve as potential recorders of flood events and could be used for flood-frequency analysis. The study of the Fares sinkhole via trenching illustrates the main limitations of sinkholes located in floodplains as archives for floods. (1) incomplete records: rapid aggradation by frequent floods overwhelms subsidence, limiting the potential for the accumulation of flood deposits unless sinkholes are affected by high subsidence rates; and (2) radiocarbon dating does not have sufficient resolution for resolving the timing of floods with decadal recurrence periods. These problems could be partially overcome by selecting relatively old sinkholes located in low terraces or benches where, fine-grained slackwater deposits may accumulate during low-frequency high-stage floods. These flood deposits may not be suitable as paleostage indicators due to section instability and post-sedimentary subsidence, but could provide insights into the timing and recurrence of large-magnitude floods

Acknowledgements

This work has been supported by project CGL2017-85045-P (Ministerio de Ciencia, Innovación y Universidades, Gobierno de España). We would like to thank Isidre Xiqués and Juan Planes from Cal Tit for giving permission to excavate trenches in the Fares and Anfiteatro sinkholes, respectively. Also to Institut Cartogràfic i Geològic de Catalunya (ICGC) and Agència Catalana de l'Aigua (ACA) for providing copies of unpublished geotechnical reports. I.F. has a FPI grant (BES-2014-068836) of the Spanish Government. M.Z. has a Serra Húnter fellowship at the Universitat Autònoma de Barcelona (UAB).

References

ACA., 2011. Avaluació preliminar del risc d'inundació del districte de conca fluvial de Catalunya (APRI). Annex 4: Anàlisis de les inundacions històriques. Apèndix 4A02: Llistat inundacions històriques a nivell de conca. Generalitat de Catalunya, Departament de Territori i Sostenibilitat. Barcelona. (60 p). Retrieved from http://aca-web.gencat.cat/aca/documents/ca/publicacions/espais_fluvials/estudis/CICP0037/09038_04A02_Llistat_conca_vd.pdf. Consulted the [06/17/2018].

ACA., 2018. Catàleg de descàrrega cartogràfica. Consulta de dades. Agència Catalana de l'Aigua. Generalitat de Catalunya. Departament de Territori i Sostenibilitat. Barcelona. Consulted the [06/17/2018].

Annan, A., 2009. Electromagnetic principles of Ground Penetrating Radar. In: Hol. J.M. (Ed.), Ground Penetrating Radar: Theory and Applications. Springer, pp. 3-40.

Ashley, G.M., 1990. Classification of the large-scale subaqueous bedforms: a new look at an old problema Journal of Sedimentary Petrology 60, 160-172.

Barberà, M., Buxó, P., 1998. Estudi sobre la possibilitat de moviments del terreny a la població de Besalú i les rodalies (Garrotxa). Institut Cartogràfic de Catalunya. AR-083-98. (40 pp.). (Unpublished report).

Barnolas, A., Pujalte, V., 2004. La Cordillera Pirenaica. Definición, límites y división. In: Vera, J.A. (Ed.), Geología de España. Sociedad Geológica de España – IGME, Madrid, pp. 233–241.

Barreiro-Lostres, F., Moreno, A., Giralt, S., Caballero, M., Valero-Garcés, B., 2014. Climate, palaeohydrology and land use change in the Central Iberian Range over the last 1.6 kyr: The La Parra Lake record. The Holocene 24, 1177-1192.

Benito, G., Sánchez-Moya, Y., Sopeña, A., 2003. Sedimentology of high-stage flood deposits of the Tagus River, Central Spain. Sedimentary Geology 157, 107-132.

Burch, J., Casas, J., Castanyer, P., Costa, A., Nolla, J.M., Palahí, L., Sagrera, J., Simon, J., Tremoleda, J., Varenna, A., Vivó, D., Vivo, J., 2014. L'Alt Imperi al nord-est del "Conuentus Tarraconensis": Una visió de conjunt. Documenta Universitaria, Institut de Recerca Històrica, Laboratori d'Arqueologia i Prehistòria, Universitat de Girona, Girona. (495 pp.). (Unpublished report).

Brown, A.L., Reinhardt, E.G., van Hengstum, P.J., Pilarczyk, J.E., 2014. A coastal Yucatan sinkhole records intense hurricane events. Journal of Coastal Research 30, 418-428.

Calvo, J.P., Pozo, M., Silva, P.G., Morales, J., 2013. Pattern of sedimentary infilling of fossil mammal traps formed in pseudokarst at Cerro de los Batallones, Madrid Basin, central Spain. Sedimentology 60, 1681-1708.

Carbonel, D., Rodríguez, V., Gutiérrez, F., McCalpin, J.P., Linares, R., Roqué, C., Zarroca, M., Guerrero, J., Sasowsky, I., 2014. Evaluation of trenching, ground penetrating radar (GPR) and electrical resistivity tomography (ERT) for sinkhole characterization. Earth Surface Processes and Landforms 39, 214-227.

Carbonell, E., Bermúdez de Castro, J.M., Parés, J.M., Pérez-González, A., Cuenca-Bescos, G., Ollé, A., Mosquera, M., Huguet, R., van der Made, J., Rosas, A., Sala, R., Vallverdú, J., García, N., Granger, D.E., Martinón-Toeers, M., Rodríguez, X.P., Stock, G.M., Vergès, J.M., Allué, E., Burjachs, F., Cáceres, I., Canals, A., Benito, A., Díez, C., Lozano, M., Mateos, A., Navazo, M., Rodríguez, J., Rosell, J., Arsuaga, J.L., 2008. The first hominid of Europe. Nature 452, 465-469.

Carrillo, E., Rosell, L., Ortí, F., 2014. Multiepisodic evaporite sedimentation as an indicator of paleogeographical evolution in foreland basins (South-eastern Pyrenean basin, Early-Middle Eocene). Sedimentology 61, 2086–2112.

Casas, J., Nolla, J.M., Prat, M., 2016. Memòria d'excavació al Camp de l'Olla. Laboratori d'Arqueologia i Prehistòria del Institut de Recerca Històrica, Universitat de Girona, Girona (20 pp.). (Unpublished report).

CTEI., 1985. Estudio de inundaciones históricas: Mapa de riesgos potenciales. Comisión Técnica de Emergencia por Inundaciones, Comisión Nacional de Protección Civil,

Fabregat, I., Gutiérrez, F., Roqué, C., Comas, X., Zarroca, M., Carbonel, D., Guerrero, J., Linares, R., 2017. Reconstructing the internal structure and long-term evolution of hazardous sinkholes combining trenching, electrical resistivity imaging (ERI) and ground penetrating radar (GPR). Geomorphology 285, 287–304.

Gischler, E., Shinn, E.A., Oschmann, W., Fiebig, J., Buter, N.A., 2008. A 1500-yr Holocene Caribbean climate archive from the Blue Hole, Lighthouse Reef, Belize. Journal of Coastal Research 24, 1495-1505.

Gutiérrez, F., 2016. Sinkhole hazards. Oxford Research Encyclopedia of Natural Hazard Science. Oxford University Press, Oxford.

Gutiérrez, F., Guerrero, J., Lucha, P., 2008. A genetic classification of sinkholes illustrated from evaporite paleokarst exposures in Spain. Environmental Geology 53, 993–1006.

Gutiérrez, F., Galve, J.P., Lucha, P., Bonachea, J., Jordá, L., Jordá, R., 2009. Investigation of a large collapse sinkhole affecting a multi-storey building by means of geophysics and the trenching technique (Zaragoza city, NE Spain). Environmental Geology 58(5), 1107-1122.

Gutiérrez, F., Zarroca, M., Castañeda, C., Carbonel, D., Guerrero, J., Linares, R., Roqué, C., Lucha, P., 2017. Paleoflood records from sinkholes using an example from the Ebro River floodplain, northeastern Spain. Quaternary Research 88(1), 71–88.

Gutiérrez, F., Zarroca, M., Linares, R., Roqué, C., Carbonel, D., Guerrero, J., McCalpin, J.P., Comas, X., Cooper, A.H., 2018. Identifying the boundaries of sinkhole and subsidence areas and establishing setback distances. Engineering Geology, 233, 255-268.

Gutiérrez, F, Fabregat, I., Roqué, C., Carbonel, D., Guerrero, J., García-Hermoso, F., Zarroca, M., Linares, R., 2016. Sinkholes and caves related to evaporite dissolution in a stratigraphically and structurally complex setting, Fluvia Valley, eastern Spanish Pyrenees. Geological, geomorphological and environmental implications. Geomorphology 267, 76–97.

Gutiérrez, F, Fabregat, I., Roqué, C., Carbonel, D., Zarroca, M., Linares, R., Yechieli, Y., García-Arnay, J., Sevil, J. 2019. Sinkholes in hypogene versus epigene karst systems, illustrated with the hypogene gypsum karst of the Sant Miquel de Campmajor Valley, NE Spain. Geomorphology 328, 57–78.

Hart, E.A., 2014. Legacy sediment stored in sinkholes: a case study of three urban watersheds in Tennessee, United States of America. Physical Geography 35, 514-531.

Hoddel, D.A., Brenner, M., Curtis, J.H., Medina-González, R., 2005. Climate change on the Yucatan Peninsula during the Little Ice Age. Quaternary Research 63, 109-121.

Hyatt, J.A., Gilbert, R., 2004. Subbottom acoustic and sedimentary records of past surface water-groundwater exchange through sinkhole lakes in South Georgia, USA. Environmental Geology 46, 32-46.

ICC., 2001. Avaluació i zonació de la perillositat d’esfondraments al municipi de Besalú. Informe ICC AR-085-01. Institut Cartogràfic de Catalunya, Generalitat de Catalunya. 291p. (Unpublished report).

ICC., 2010. Estudi de perillositat enfront esfondraments a Beuda (Garrotxa). Informe IGC AP-043/10. Institut Cartogràfic de Catalunya, Generalitat de Catalunya. 142p. (Unpublished report).

ICGC., 2018. Visualitzador Geoíndex Sondejos. Institut Cartogràfic i Geològic de Catalunya, Generalitat de Catalunya [http://www.icgc.cat/geoindex]

Johnson, S.Y., 1986. Water-scape structures in coarse-grained, volcanoclastic, fluvial deposits of the Ellensburg Formation, South-Central Washington. Journal of Sedimentary Petrology 56, 905-910

Kovacs, S.E., van Hengstum, P.J., Reinhardt, E.G., Donnelly, J.P., Albury, N.A., 2013. Late Holocene sedimentation and hydrologic development in a shallow coastal sinkhole on Great Abaco Island, The Bahamas. Quaternary International 317, 118-132.

Kulkarni, C., Peteet, D., Boger, R., Heusser, L., 2016. Exploring the role of humans and climate over the Balkan landscape: 500 years of vegetational history of Serbia. Quaternary Science Reviews, 144, 83-94.

Lane, P., Donnelly, J.P., Woodruff, J.D., Hawkes, A.D., 2011. A decadally-resolved paleohurricane record archived in the late Holocene sediments of a Florida sinkhole. Marine Geology 287, 14-30.

Laury, R. L., 1980. Paleoenvironment of a late Quaternary mammoth-bearing sinkhole deposit, Hot Springs, South Dakota. Geological Society of America Bulletin 91, 465-475.

Lejarza, J.R., (2017, April 15). El Pont Medieval de Besalú compleix sis-cents anys. El Garrotxí.cat, Diari digital de la Garrotxa. Retrieved from http://www.elgarrotxi.cat/el-pont-medieval-de-besalu-compleix-sis-cents-anys/

Lewis, C.J., Balbridge, W.S., Asmerom, Y., 1998. Neogene asthenosphere derived volcanism and NE-directed extension in NE Spain: Constraints on the geodynamic evolution of the western Mediterranea. Eos Trans. AGU 79(17), Spring Meeting Suppl., S336–S337.

Linares, R., Roqué, C., Gutiérrez, F., Zarroca, M., Carbonel, D., Bach, J., Fabregat, I., 2017. The impact of droughts and climate change on sinkhole occurrence. A case study from the evaporite karst of the Fluvia Valley, NE Spain. Science of The Total Environment 579, 345–358.

Field Code Changed

Llansana i Benaiges, E., 2013. La Santíssima Veracreu de Besalú. Història d´un mil·lenari (1017-2017). Biblioteca Municipal de Besalú.

Martínez, A., Rivero, L., Casas, A., 1997. Integrated gravity and seismic interpretation of duplex structures and imbricate thrust systems in the southeastern Pyrenees (NE Spain). Tectonophysics 282, 303–329.

Martínez, A., Samsó, J.M., Zamorano, M., Picart, J., Solà, J., Montaner, J., Mató, E., 2000. Besalú (76-22). Mapa Geològic de Catalunya 1:25.000. Institut Cartogràfic de Catalunya.

Martínez-Solares, J.M., Mezcua, J., 2002. Catálogo sísmico de la Península Ibérica (880 a.C.-1900). Instituto Geográfico Nacional. Madrid, 253 p.

Mató. E., Saula, E., Picart, J., Solà, J., Montaner, J., Viñals, E., Samsó, J.M., Serra, J., Llenas, M., Agustí, J., Mallarach, J., 1996. Banyoles (76-23). Mapa Geològic de Catalunya 1:25.000. Institut Cartogràfic de Catalunya. Barcelona.

Meteocat., 2018. Atles Climàtic de Catalunya. Servei Meteorològic de Catalunya. Generalitat de Catalunya. Ed. 2008. Consulted the [07/04/2018].

Miall, A.D., 1996. The Geology of Fluvial Deposits. Springer, 582 p.

Morellón, M., Valero-Garcés, B., Anselmetti, F., Ariztegui, D., Schnellmann, M., Moreno, A.N.A., Mata, P., Rico, M., Corella, J.P., 2009. Late Quaternary deposition and facies model for karstic Lake Estanya (North-eastern Spain). Sedimentology 56, 1505-1534.

Nocita, B.W., 1988. Soft-sediment deformation (fluid escape) features in a coarse-grained pyroclastic-surge deposit, north-central New Mexico. Sedimentology 35, 275-285.

Papell i Llenas, J., 1862. Provincia de Gerona. Partido judicial de Olot. Plano geométrico-topográfico de los terrenos que constituyen el distrito municipal de Besalu. 1:2000. Ayuntamiento de Besalú (Besalú). 1 mapa en 1 hoja.

Perea, H., 2009. The Catalan seismic crisis (1427 and 1428; NE Iberian Peninsula): geological sources and earthquake triggering. Journal of Geodynamics 47, 259–270.

Perrotti, A.G., 2018. Pollen and Sporormiella evidence for terminal Pleistocene vegetation change and megafaunal extinction at Page-Ladson, Florida. Quaternary International 466, 256-268.

Postma, G., 1983. Water escape structures in the context of a depositional model of a mass flow dominated conglomeratic fan-delta (Abrioja Formation, Pliocene, Almeria Basin, SE Spain). Sedimentology 30(1), 91–103.

Puigdefàbregas, C., Muñoz, J.A., Marzo, M., 1986. Thrust belt development in the Eastern Pyrenees and related depositional sequences in the southern foreland basin. In: Allen, P.A., Homewood, P. (Eds.), Foreland Basins. International Association of Sedimentologists Special Publication 8, 229–246.

Reimer, P. J., Bard, E., Bayliss, A., Beck, J. W., Blackwell, P. G., Bronk Ramsey, C., Grootes, P. M., Guilderson, T. P., Haflidason, H., Hajdas, I., HattŽ, C., Heaton, T. J., Hoffmann, D. L., Hogg, A. G., Hughen, K. A., Kaiser, K. F., Kromer, B., Manning, S. W., Niu, M., Reimer, R. W., Richards, D. A., Scott, E. M., Southon, J. R., Staff, R. A., Turney, C. S. M., and van der Plicht, J., 2013. IntCal13 and Marine13 Radiocarbon Age Calibration Curves 0-50,000 Years cal BP. Radiocarbon 55, 1869–1887.

Roqué, C., Pallí, L., Capellà, I., Linares, R., Brusi, D., 1999. Els esfondraments per carstificació al terme municipal de Besalú. La Punxa 28, 42–53.

Sevil, J., Gutiérrez, F., Zarroca, M., Desir, G., Carbonel, D., Guerrero, J., Linares, R., Roqué, C., Fabregat, I., 2017. Sinkhole investigation in an urban area by trenching in combination with GPR, ERT and high-precision leveling. Mantled evaporite karst of Zaragoza city, NE Spain. Engineering Geology, 231, 9-20.

Siart, C., Hecht, S., Holzhauer, I., Altherr, R., Meyer, H.P., Schukraft, G., Eitel, B., Bubenzer, O., Panagiotopoulos, D., 2010. Karst depressions as geoarchaeological archives: The palaeoenvironmental reconstruction of Zominthos (Central Crete), based on geophysical prospection, sedimentological investigations and GIS. Quaternary International, 216, 75-92.

Stuiver, M., Reimer, P.J., 1993. Extended 14C database and revised CALIB 3.0 14C age calibration program, Radiocarbon 35, 215–230.

Stuiver, M., Reimer, P.J., Reimer, R.W., 2017, CALIB 7.1 (www program) at http://calib.org.

Turnage, K.M., Lee, S.Y., Foss, J.E., Kim, K.H., Larsen, I.L., 1997. Comparison of soil erosion and deposition rates using radiocesium, RUSLE, and buried soils in dolines in East Tennessee. Environmental Geology 29, 1-10.

Van Hengstum, P.J., Maale, G., Donnelly, J.P., Albury, N.A., Onac, B.P., Sullivan, R.M., Winkler, T.S., Tamalavage, A.E., MacDonald, D., 2018. Drought in the northern Bahamas from 3300 to 25000 years ago. Quaternary Science Reviews 186, 169-185.Whitmore, T.J., Brenner, M., Curtis, J.H., Dahlin, B.H., Leyden, B.W., 1996. Holocene climatic and human influences on lakes of the Yucatan Peninsula, Mexico: an interdisciplinary, palaeolimnological approach. The Holocene 6, 273-287.

Youssef, A.M., Al-Harbi, H.M., Gutiérrez, F., Zabramwi, Y.A., Bulkhi, A.B., Zahrani, S.A., Bahamil, A.M., Zahrani, A.J., Otaibi, Z.A., El-Haddad, B.A., 2016. Natural and human-induced sinkhole hazards in Saudi Arabia: distribution, investigation, causes and impacts. Hydrogeology Journal 24(3), 625-644.

Zaidner, Y., Frumkin, A., Porat, N., Tsatskin, A., Yeshurun, R., Weissbrod, L., 2014. A series of Mousterian occupations in a new type of site: The Nesher Ramla karst depression, Israel. Journal of Human Evolution 66, 1-17.

Figure captions

Figure 1. General geological and geomorphological setting of the study area. (A): Location of the study area within the geological context of the Pyrenees. (B): Shaded relief model showing the position of the analysed sinkholes in the northern sector of the Ebro Cenozoic Basin, south of the N-dipping Vallfogona Thrust. (C): Synthetic stratigraphic section of the Eocene stratigraphic units exposed in the area. The studied sinkholes are related to interstratal karstification of the Beuda Gypsum underlying a thick caprock of Banyoles Marls.

Figure 2. Geomorphic setting of the Anfiteatro sinkhole, trenching and GPR investigation layout. A: Annotated oblique aerial view of the Anfiteatro sinkhole. B: Detailed geomorphological map of the sinkhole site.

Figure 3. Log and description of stratigraphic units of the Anfiteatro trench. Inset photograph shows the marginal collapse fault that juxtaposes packages I and II and that is onlapped by package III. Note gravel pocket in the upper part of package II. Numerical ages are calibrated radiocarbon dates with 2 sigma uncertainty.

Figure 4. Chronological model generated with the numerical age ranges (2 sigma uncertainty) and the overlying sediment thickness.

Figure 5. Retrodeformation analysis of the Anfiteatro trench. For simplicity, it assumes that the collapsed terrace deposit in the downthrown block is situated just beneath the base of the trench. See explanation in the text.

Figure 6. Geophysical data from the Anfiteatro sinkhole. See location of profiles in figure 2. A: Structural sketch of the trench. B: GPR profile acquired with the 100 MHz shielded antenna.

Figure 7. Geomorphic setting of the Fares sinkhole and layout of the trenching and GPR investigation. The figure indicates the trace of the GPR profile presented in figure 11A.

Figure 8. Log and description of stratigraphic units of the Fares trench. Numerical ages are calibrated radiocarbon dates with 2 sigma uncertainty.

Figure 9. Images of the Fares trench. A: General view of the southern wall of the trench exposing a collapse sinkhole with internal sagging deformation. B: Fining-upward flood sequence corresponding to package II on the western, upstream margin of the sinkhole. C: Close-up view of the eastern margin of the collapse. D: Close-up view of the western margin of the collapse.

Figure 10. Retrodeformation analysis of the Fares trench.

Figure 11. Geophysical data of the Fares sinkhole. A: GPR profile acquired with the 40 MHz unshielded antenna. Location of the trench on the left and interpretation of the radargram on the right. B: Stratigraphic and structural sketch of the Fares trench

Fig. 1

Click here to access/download;Figure;Figura1_General-01_revised.jpg

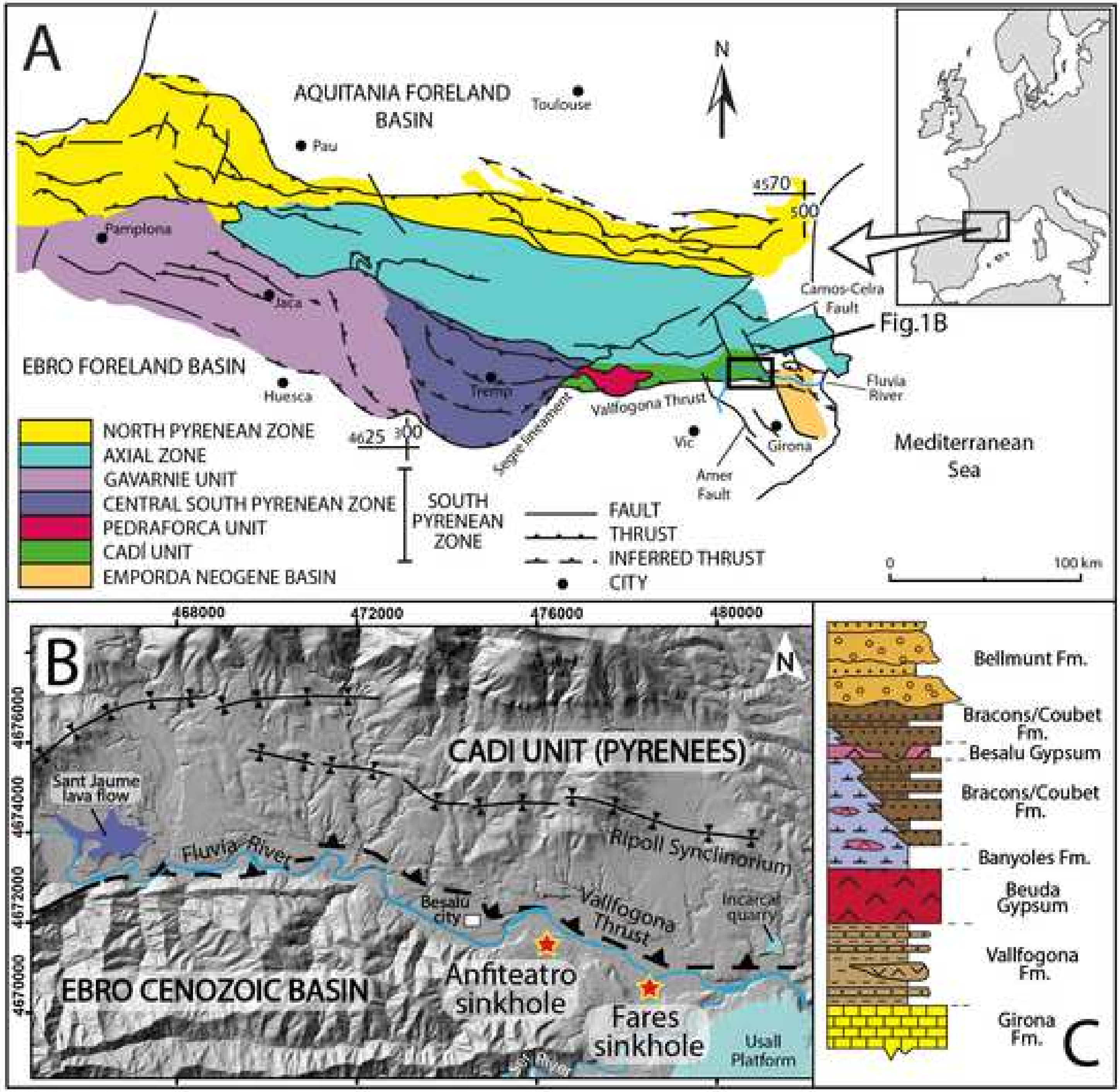

Fig. 2

Click here to access/download;Figure;Fig 2. New.jpg

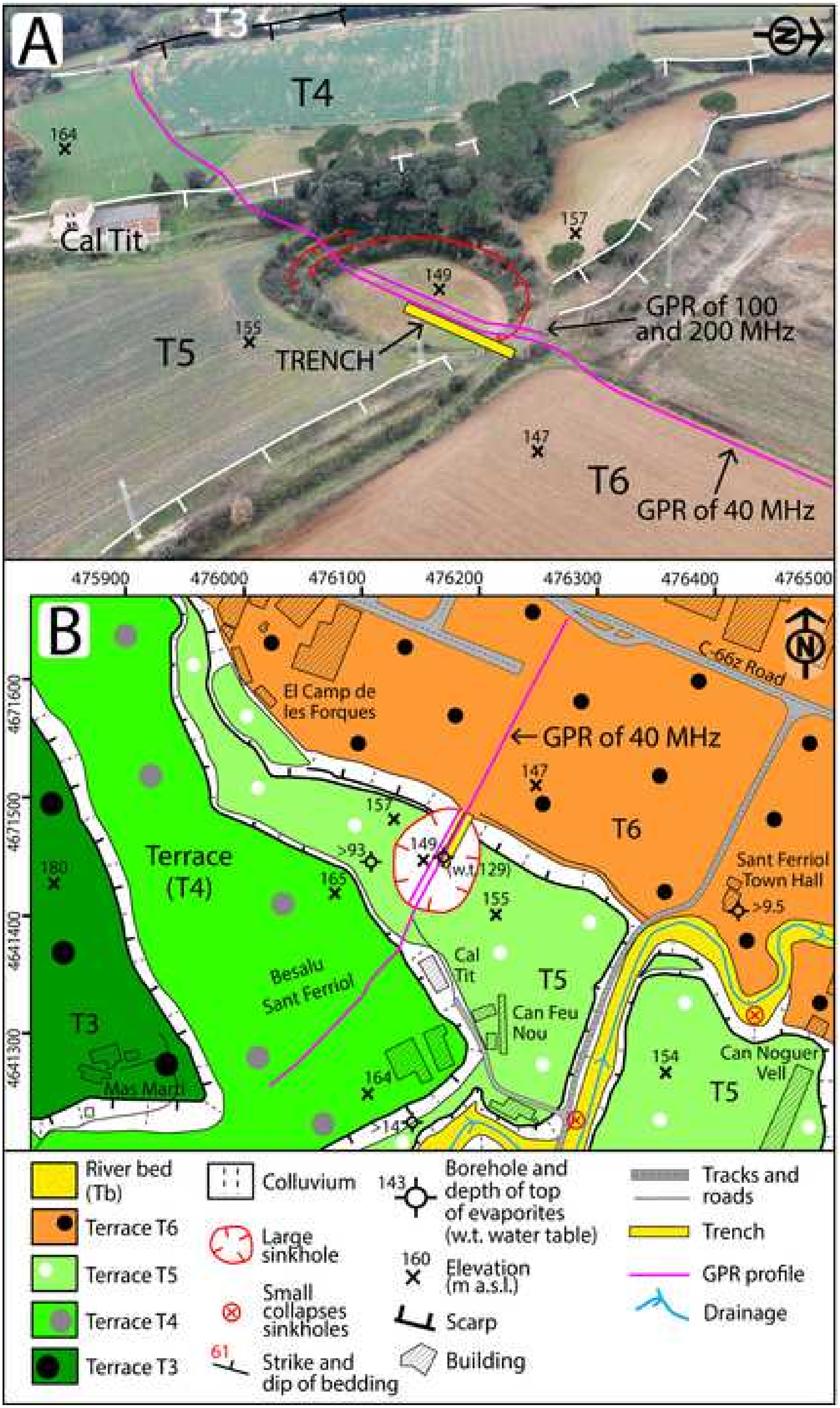

Fig. 3

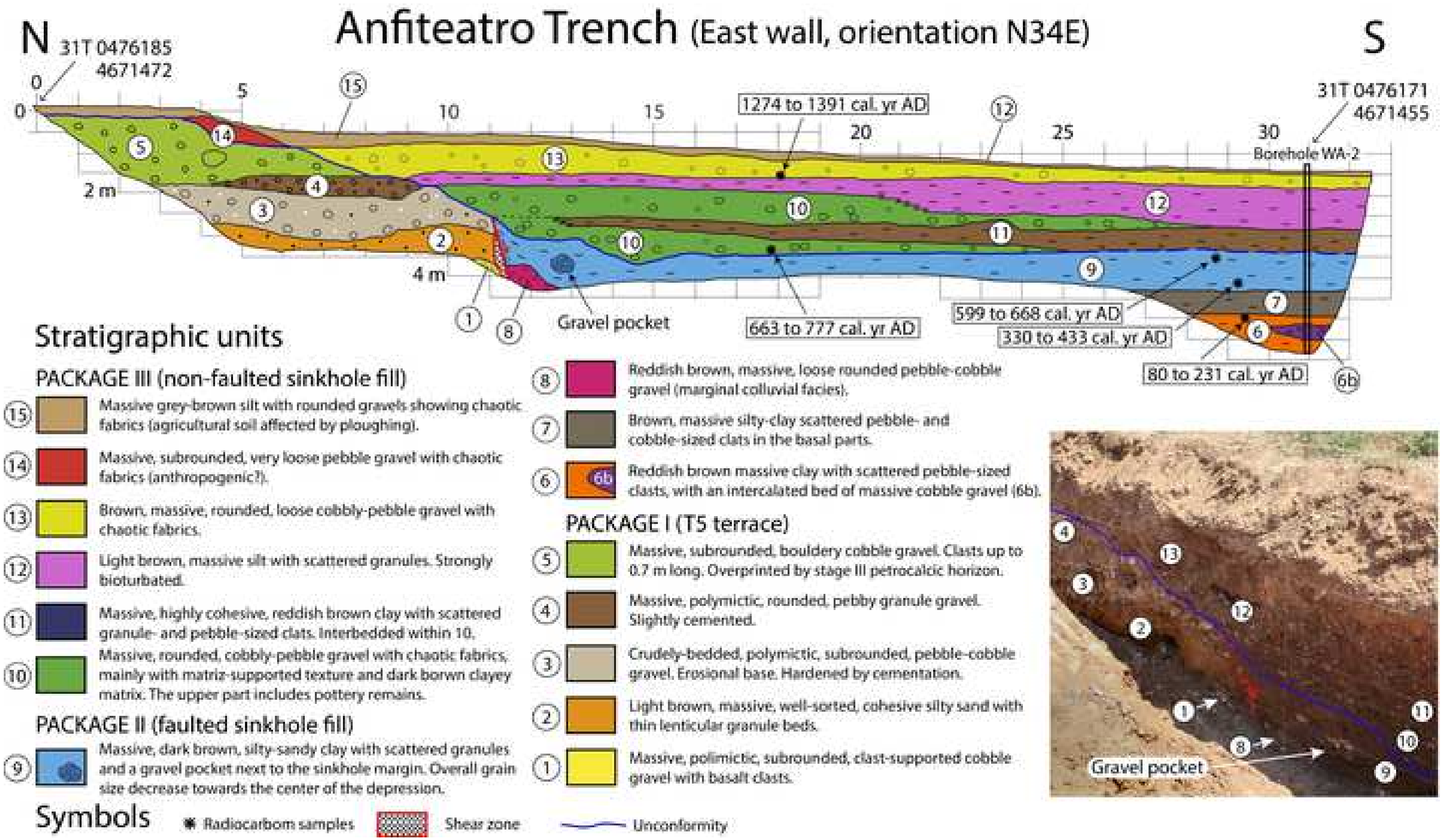
Anfiteatro Trench (East wall, orientation N34E)
N
S
31T 0476185
4671472
31T 0476171
4671455
Borehole WA-2
0
5
10
15
20
25
30
2 m
4 m
1274 to 1391 cal. yr AD
663 to 777 cal. yr AD
599 to 668 cal. yr AD
330 to 433 cal. yr AD
80 to 231 cal. yr AD
Gravel pocket
Stratigraphic units
PACKAGE III (non-faulted sinkhole fill)
15 Massive grey-brown silt with rounded gravels showing chaotic fabrics (agricultural soil affected by ploughing).
14 Massive, subrounded, very loose pebble gravel with chaotic fabrics (anthropogenic?).
13 Brown, massive, rounded, loose cobbly-pebble gravel with chaotic fabrics.
12 Light brown, massive silt with scattered granules. Strongly bioturbated.
11 Massive, highly cohesive, reddish brown clay with scattered granule- and pebble-sized clats. Interbedded within 10.
10 Massive, rounded, cobbly-pebble gravel with chaotic fabrics, mainly with matriz-supported texture and dark borwn clayey matrix. The upper part includes pottery remains.
PACKAGE II (faulted sinkhole fill)
9 Massive, dark brown, silty-sandy clay with scattered granules and a gravel pocket next to the sinkhole margin. Overall grain size decrease towards the center of the depression.
8 Reddish brown, massive, loose rounded pebble-cobble gravel (marginal colluvial facies).
7 Brown, massive silty-clay scattered pebble- and cobble-sized clats in the basal parts.
6 6b Reddish brown massive clay with scattered pebble-sized clasts, with an intercalated bed of massive cobble gravel (6b).
PACKAGE I (T5 terrace)
5 Massive, subrounded, bouldery cobble gravel. Clasts up to 0.7 m long. Overprinted by stage III petrocalcic horizon.
4 Massive, polymictic, rounded, pebby granule gravel. Slightly cemented.
3 Crudely-bedded, polymictic, subrounded, pebble-cobble gravel. Erosional base. Hardened by cementation.
2 Light brown, massive, well-sorted, cohesive silty sand with thin lenticular granule beds.
1 Massive, polimictic, subrounded, clast-supported cobble gravel with basalt clasts.
Symbols
Radiocarbom samples
Shear zone
Unconformity

Fig 4

Click here to access/download;Figure;Fig. 4. Graph of Anfiteatro.jpg

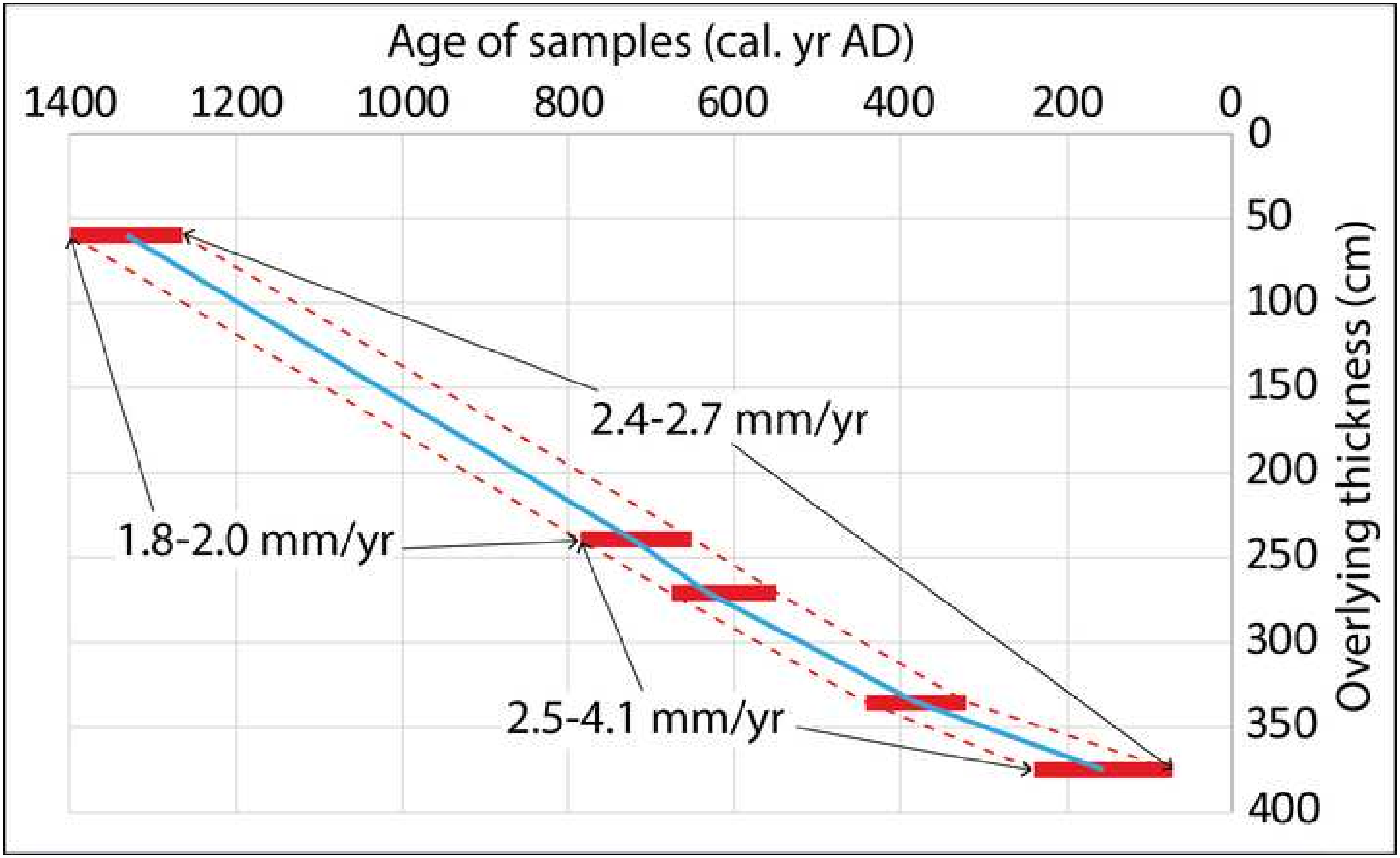

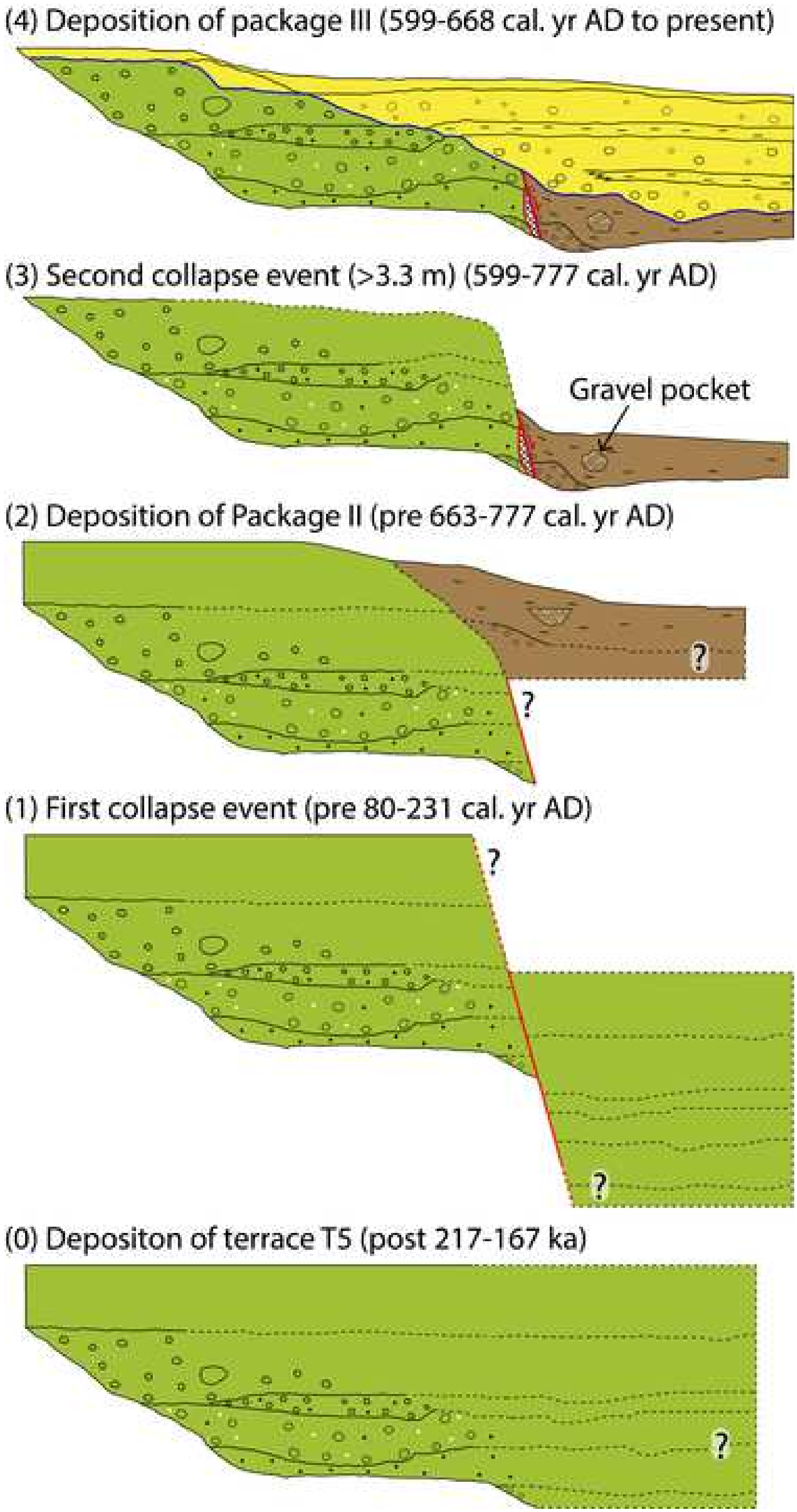
(4) Deposition of package III (599-668 cal. yr AD to present)
(3) Second collapse event (>3.3 m) (599-777 cal. yr AD)
Gravel pocket
(2) Deposition of Package II (pre 663-777 cal. yr AD)
?
?
(1) First collapse event (pre 80-231 cal. yr AD)
?
?
(0) Depositon of terrace T5 (post 217-167 ka)
?

Fig. 6

Click here to access/download;Figure;Fig 6. New.jpg

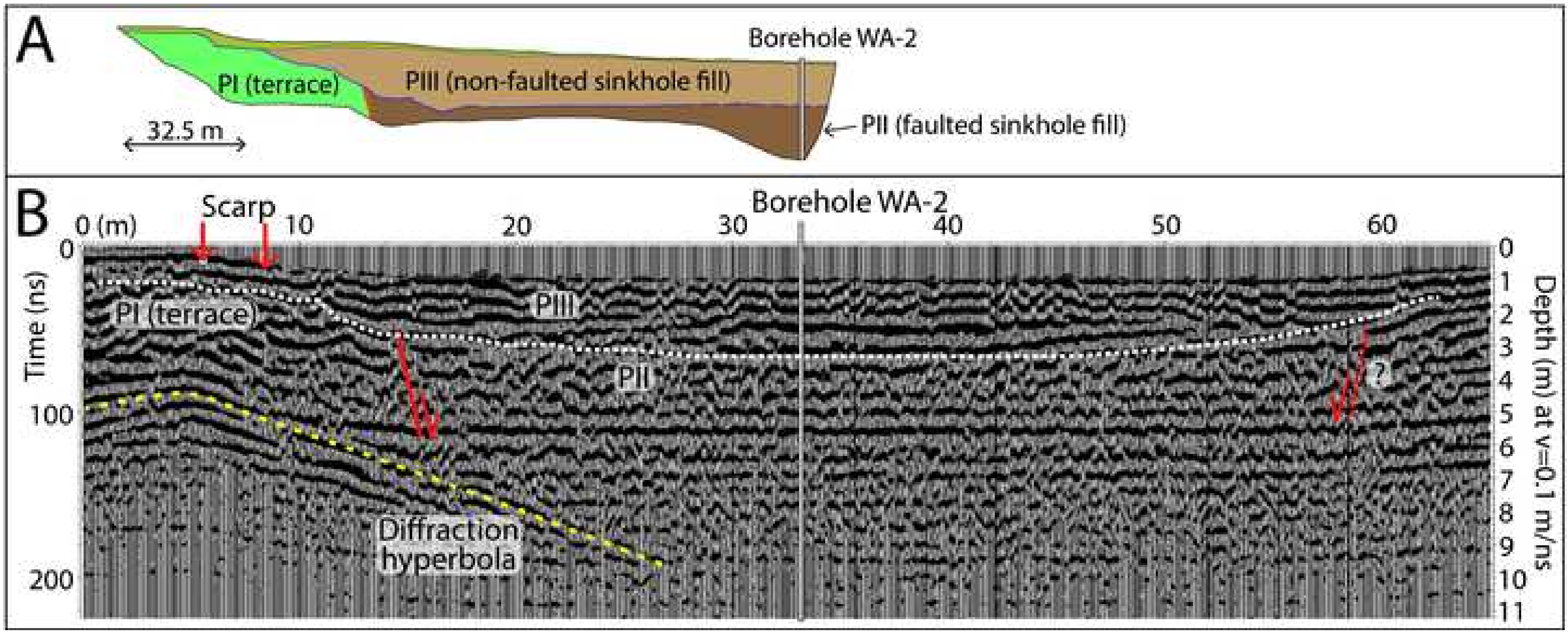

Fig. 7

Click here to access/download;Figure;Fig 7. New.jpg

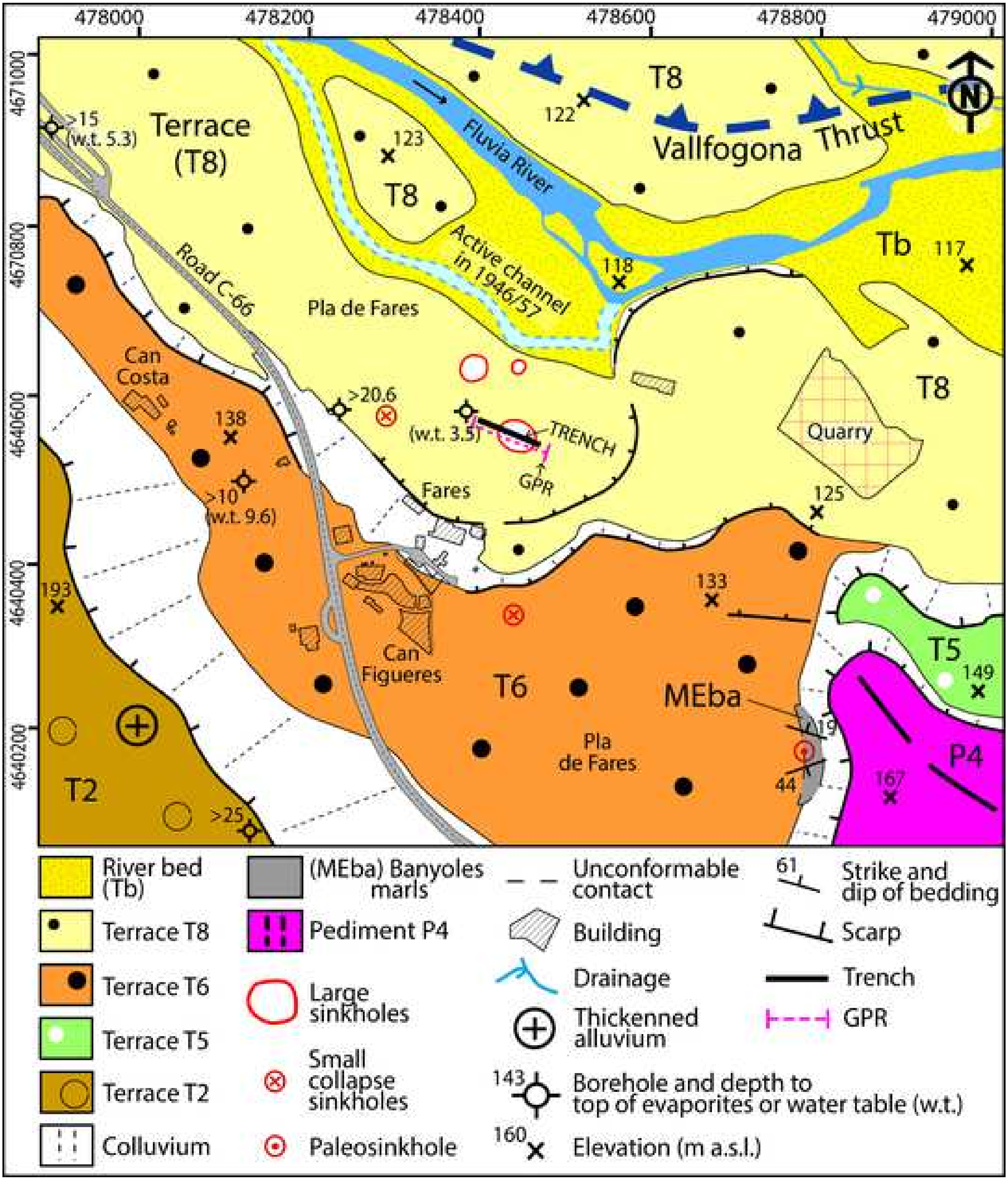

Fig. 8

Click here to access/download;Figure;Fig. 8. Trinchera Fares.jpg

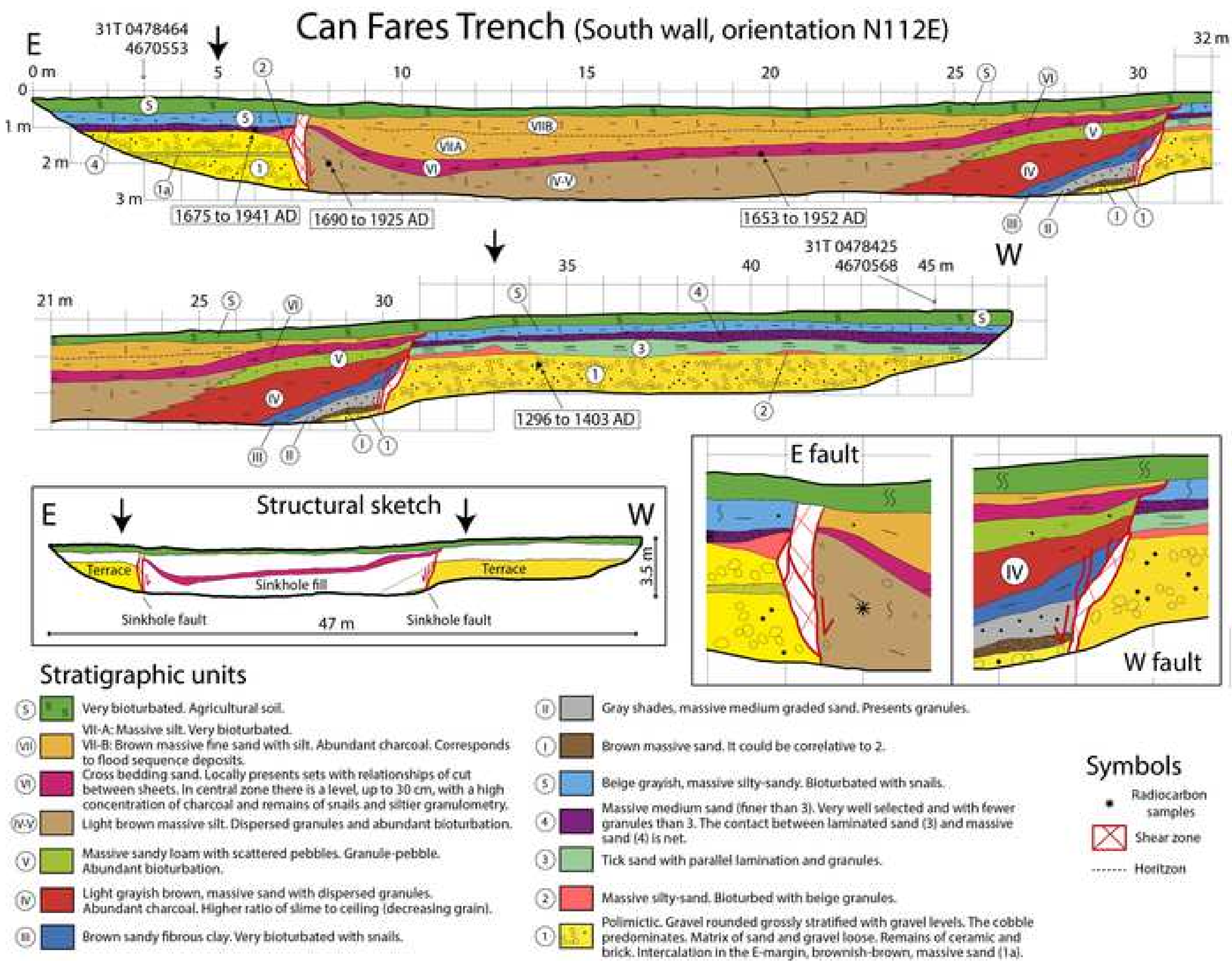

Fig. 9

Click here to access/download;Figure;Fig. 9. Imagenes_Fares.jpg

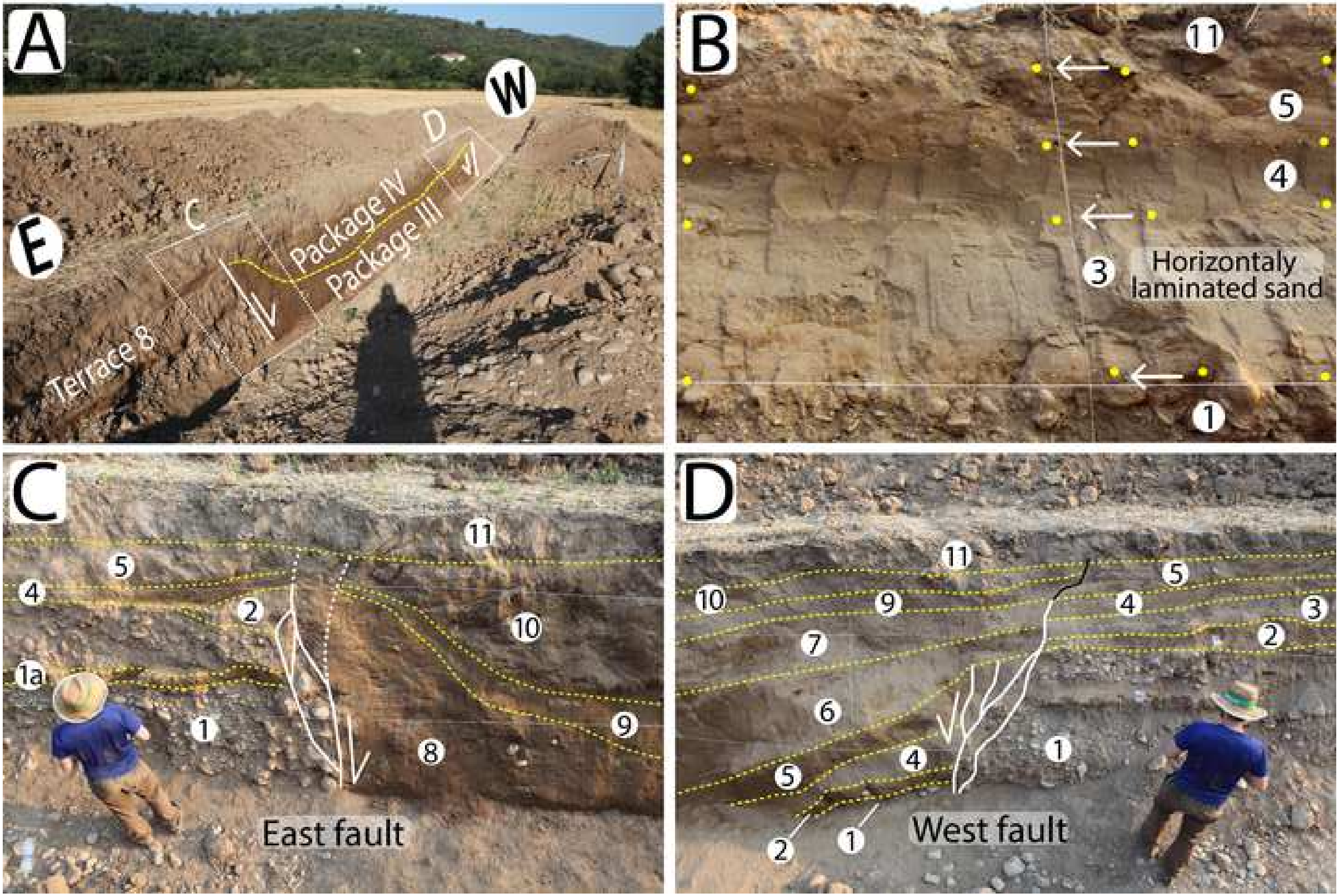

Fig. 10

Click here to access/download;Figure;Fig. 10. Retrodeformacion Fares.jpg

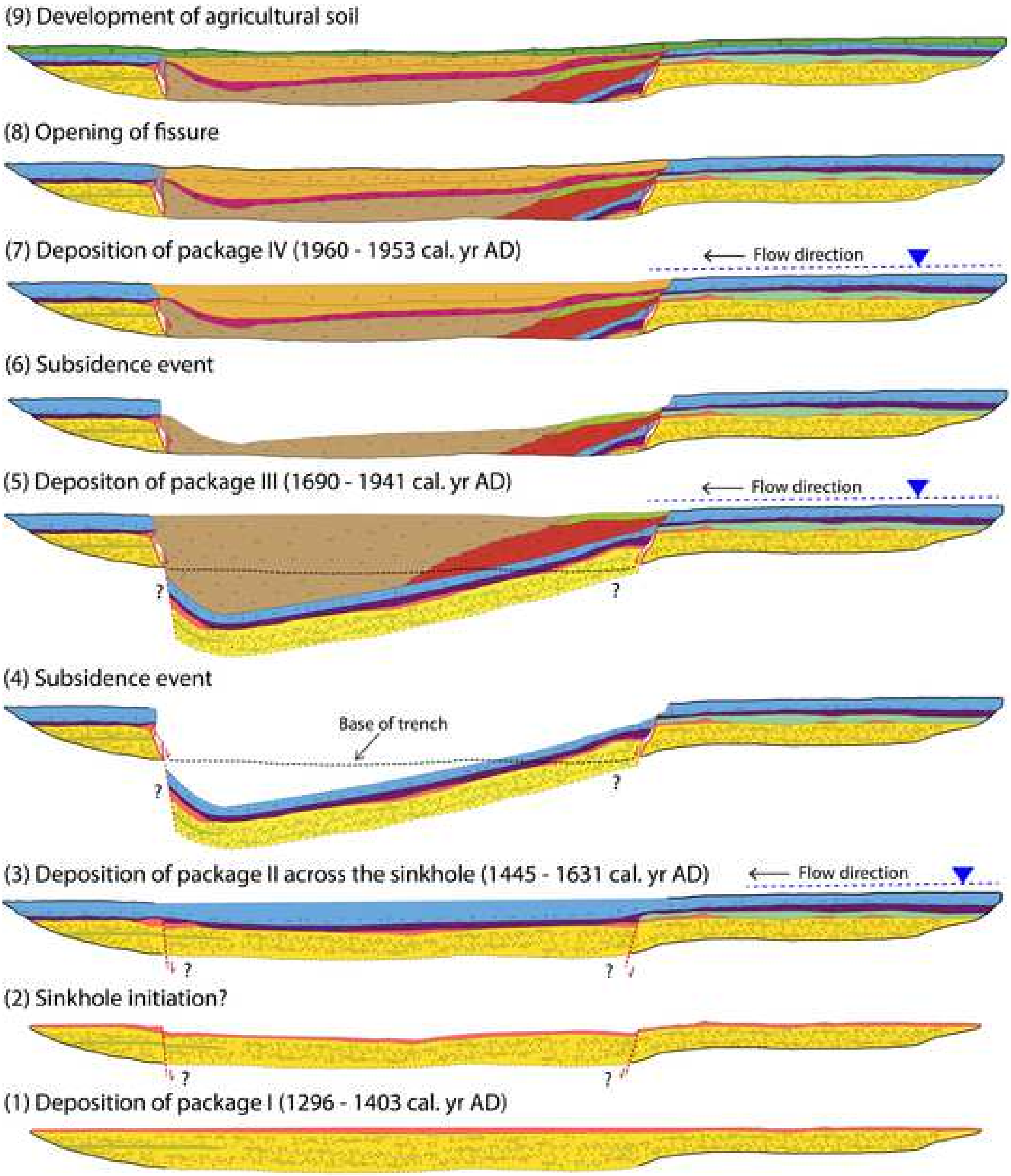

Fig. 11

Click here to access/download;Figure;Fig 11. New.jpg

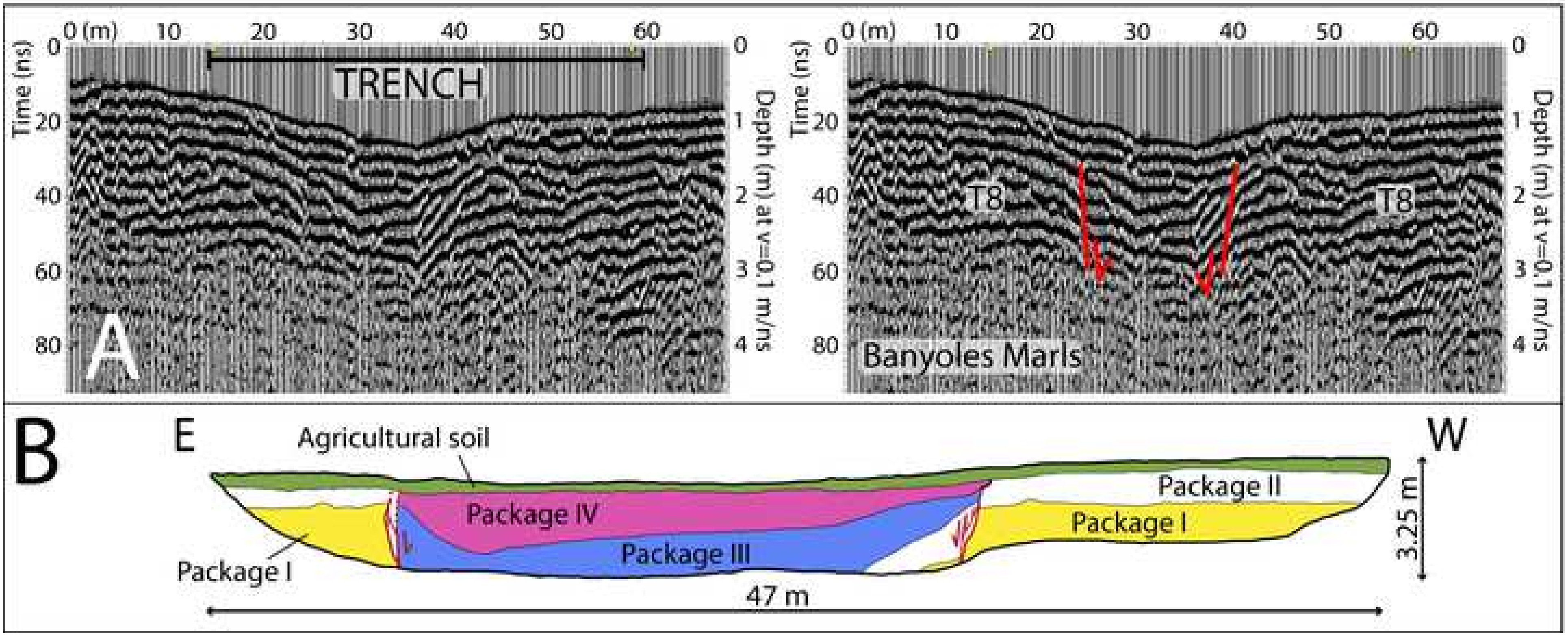

Table 1

Table 2

Click here to access/download
Table
Table 2revised.docx